Thin–Walled Structures 205 (2024) 112602

Contents lists available at ScienceDirect

Thin-Walled Structures

journal homepage: www.elsevier.com/locate/tws

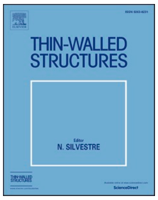

Residual behaviour and damage assessment of UHPC-filled double-skin steel tubular columns after lateral impact

Weiqiang Wang [a], Zhilong Xiong [a], Yang Yu [b,*], Da Chen [c], Chengqing Wu [d]

[a] College of Water Conservancy and Hydropower Engineering, Hohai University, Nanjing 210098, China
[b] Centre for Infrastructure Engineering and Safety, School of Civil and Environmental Engineering, University of New South Wales, Sydney, NSW 2052, Australia
[c] College of Harbour, Coastal and Offshore Engineering, Hohai University, Nanjing 210098, China
[d] Centre for Built Infrastructure Research, School of Civil and Environmental Engineering, University of Technology Sydney, Sydney, NSW 2007, Australia

ARTICLE INFO

Keywords:
UHPC
CFDST columns
Impact height
Damage index
Machine learning

ABSTRACT

Ultra-high performance concrete (UHPC)-filled double-skin steel tubular (DST) column has great potential to be used in the protective structures. Although its lateral impact behaviour has been well understood, the residual behaviour after lateral impact remains unexplored. As a result, this study extensively investigated the residual behaviour and damage assessment of UHPC-filled DST columns after lateral impact. Firstly, a set of six DST columns were designed and tested under lateral impact, followed by static axial compression. In addition, two intact columns were subjected to static axial compression for comparative analysis. Secondly, the refined finite element models were developed and validated using the current test data, and the impact resistant mechanism of UHPC-filled DST columns with different impact locations was analysed. Thirdly, the suitability of different damage indexes for the damage assessment of impacted UHPC-filled DST columns was evaluated. Two damage indexes, the ratio of mid-height deflection to column height (R_1), and the ratio of local deflection to the column diameter (R_2), were proposed for the DST columns. Finally, two types of machine learning-based models were developed to predict the impact damage of UHPC-filled DST columns. The prediction models were interpreted locally and globally using the additive feature attribution method Shapley Additive Explanation (SHAP). The machine learning-based prediction models can rapidly evaluate the damage extent of impacted UHPC-filled DST column, which hold great significance for the selection of strengthening and retrofitting schemes.

1. Introduction

As a variable form of concrete-filled steel tubular (CFST) column, concrete-filled double-skin steel tubular (CFDST) column consisted of two concentrically placed steel tubes while the interstice filled with concrete [1]. In the CFDST column, the concrete's strength and ductility increase significantly with constraining effect by the two steel tubes [2]. Additionally, the presence of infilled concrete can effectively limit the local buckling of steel tubes [3]. The superior performances of CFDST columns under different loading conditions have been demonstrated in numerous studies [2–9]. Nowadays, CFDST columns have been found extensive applications in offshore platforms, bridges, transmission towers, and high-rise buildings [10].

Ultra-high performance concrete (UHPC) has become increasingly popular as a result of its unique properties, including ultra-high strength, toughness, abrasion resistance, and increased durability [11]. UHPC usually features with high binder content and low water-to-cement ratio, and fibres are always added into the matrix to alleviate the brittleness and increase its energy absorption capacity [12]. Due to its excellent mechanical properties and durability, the incorporation of UHPC in the CFDST column can yield numerous advantages over the CFDST column with normal strength concrete (NSC), in particular the higher stiffness and load carrying capacity [13]. Therefore, the CFDST column's cross-sectional area can be effectively reduced by using the UHPC, leading to an increase in the available space of the structure, and thus bring more economic benefits in practical applications [14].

The CFDST columns may encounter accidental lateral impacts during their service life due to vehicle or ship collisions. Numerous studies have been undertaken to explore the dynamic reactions of CFDST columns when subjected to such impacts [15–27]. In general, the CFDST columns exhibit highly ductile behaviour against the lateral impact, and the impact force-time history usually compose of three stages during the

---

* Corresponding author.
E-mail address: yang.yu12@unsw.edu.au (Y. Yu).

https://doi.org/10.1016/j.tws.2024.112602
Received 5 May 2024; Received in revised form 10 September 2024; Accepted 17 October 2024
Available online 19 October 2024

impact: initial ascending stage, plateau stage, and unloading stage [16]. Also, the effects of various design variables on the lateral impact behaviour of CFDST columns have been extensively investigated in these studies. Moreover, except for the NSC, various types of concrete, including ultra-lightweight cement composite (ULCC), self-consolidating concrete (SCC) and UHPC, were used for the CFDST columns, and these types of columns' impact responses were extensively investigated [17,22,24,27]. Among these studies, Wang et al. [27] investigated the lateral impact behaviour of UHPC-filled double-skin steel tubular (DST) columns. Compared to the NSC-filled DST columns, higher impact resistant capacity can be achieved, including larger peak/plateau impact force, shorter impact duration, smaller maximum/residual deflection, and less local indentation. Moreover, in order to avoid the serious local deformation at the impact area during lateral impact, the void ratio should not be higher than 0.6 [27].

Lateral impact may cause significant damage to the concrete columns, and in severe instances will result in the collapse of entire structures. Existing research primarily emphasizes the dynamic impact behaviour of concrete columns, with scant attention given to studies on their post-impact behaviour [16,28–31]. Fan et al. [28] studied the residual performance of axially loaded reinforced concrete (RC) columns after the lateral impact, and the residual axial load capacity of RC column decreases with the increase in residual mid-span deflection. Through multivariable regression analysis, an empirical formula was developed to predict the residual axial performance based on the residual mid-span deflection to span length ratio. Pan and Guo [16] numerically studied the post-impact behaviour of square CFDST columns. The residual axial load capacity of impacted square CFDST columns was predicted through a simplified formula based on the linear correlation between the mid-span deflection and the residual performance. In general, despite several studies on the post-impact behaviour of different types of concrete columns, the post-impact behaviour and damage assessment of UHPC-filled DST columns remain unexplored.

It is also noted that, for the post-impact related studies, the empirical formulae were mostly derived using the traditional data regression methods [16,28–31]. Nevertheless, considering the significant influences of multiple variables on the column's residual axial load capacity, the traditional data regression methods are not able to provide accurate predictions [32]. Nowadays, machine learning is emerging as a powerful tool to predict the residual performance of concrete columns which was injured by extreme dynamic loads [32–38]. For example, Li et al. [35] developed a damage prediction model for fibre-reinforced polymer (FRP)-strengthened RC columns after blast loads using a generic algorithm-optimized neural network. According to Zhou et al. [36], two neural network models have been developed to predict the failure mode and damage level of RC columns after blast loads. Almustafa and Nehdi [32] developed an ensemble tree-based model for the deflection prediction of RC columns after blast loads. Despite several studies on the machine learning models for the blasted RC columns, studies on the machine learning models of impacted concrete columns are far less [37,38]. Zhou et al. [37] reported that a machine learning prediction model can achieve significantly greater accuracy than current empirical models in predicting the damage of RC bridge piers caused by vehicle collisions. According to Xu et al. [38], machine learning techniques, fast Fourier transforms, and finite element simulation can be combined to predict the impact forces. The results demonstrate that the proposed machine learning-based framework is capable of predicting the duration and frequency series of impact forces with great accuracies.

Based on this background, this study examined the post-impact behaviour and damage assessment of UHPC-filled DST columns after lateral impact. Firstly, a set of six DST columns were designed and tested under lateral impact, and were subsequently tested under axial compression. Two intact columns were also tested under static axial compression for comparative analysis. Secondly, refined numerical models were developed and validated using the test data, and the impact resistant mechanism of UHPC-filled DST columns was revealed using the developed numerical model. Thirdly, the appropriate damage indexes were proposed for the damage assessment of impacted UHPC-filled DST columns. Finally, two types of machine learning-based prediction models were developed based on a large database, and the contribution of each variable to the residual axial load capacity of UHPC-filled DST columns was analysed and discussed.

2. Experimental program

2.1. Test matrix

Eight CFDST specimens (2 m in height) were designed and manufactured. The outer steel tubes had 168 mm diameter while the diameter of inner steel tubes was 95 mm. The main investigated variables include the concrete type (UHPC, NSC), thickness of outer steel tube (5 mm, 8 mm), thickness of inner steel tube (4 mm, 6 mm), impact energy (0 kJ, 12.6 kJ, 16.9 kJ), and the level of axial load (0, 200 kN). The specimen labelling has the following rules: (1) "F" indicates the applied axial load; (2) "U" and "N" indicate the type of concrete, where "U" represents UHPC and "N" represents the NSC; (3) "To" and "Ti" represents the thicknesses of outer and inner steel tubes, respectively; and (4) the drop hammer height was indicated by "H" and the number afterwards. Specimen "F-U-To5-Ti4-H4" means the preloaded UHPC-filled DST specimen, the thicknesses of outer and inner steel tubes were 5 mm and 4 mm, respectively, and the drop height of hammer was 4 m. More details of the specimens can be found in Table 1.

2.2. Specimen preparations and material properties

The UHPC utilized in this work comprised Portland cement, silica fume, quartz flour, fine silica sand, a high-efficiency water-reducing agent, water, and straight steel fibres. These steel fibres were 10 mm in length and 0.12 mm in diameter. According to the manufacturer's specifications, the elastic modulus and tensile strength of these fibres were 210 GPa and 4295 MPa, respectively. To ensure uniform dispersion and random orientation, the steel fibres were manually dispersed during the mixing process. For testing the compressive strengths of concrete, three cylinders were prepared according to the AS 1012.9 standard [39], each measuring 150 mm in diameter and 300 mm in length. The results of the axial compression tests showed that the average compressive strengths of UHPC and NSC were 136 MPa and 35 MPa, respectively. Furthermore, five steel coupons of each steel tube type were longitudinally cut and tested under tension in accordance with BS18 [40] to investigate the properties of the steel tubes. Table 2 presents the tensile test results of steel tubes.

2.3. Impact test setup and test results [27]

As shown in Fig. 1(a), the impact test setup consisted of a drop hammer system, a clamping system, and a supporting system. The drop

Table 1
Test matrix.

Specimen	Concrete type	t_o	t_i	H (m)	α (kN)
U-To5-Ti4-H3	UHPC	5	4	3	0
U-To5-Ti4-H4	UHPC	5	4	4	0
U-To8-Ti4-H4	UHPC	8	4	4	0
U-To5-Ti6-H4	UHPC	5	6	4	0
F-U-To5-Ti4-H4	UHPC	5	4	4	200
N-To5-Ti4-H4	NSC	5	4	4	0
U-To5-Ti4-H0	UHPC	5	4	-	0
N-To5-Ti4-H0	NSC	5	4	-	0

Note: t_o indicates the thickness of the outer steel pipe, t_i indicates the thickness of the inner steel pipe, H indicates the impact height, and the α indicates the axial load.

Table 2
Mechanical properties of steel tubes.

Size (mm)	Yield stress (MPa)	Ultimate strength (MPa)	Elastic modulus (GPa)	Elongation at break
95 × 4	310	385	200	23%
95 × 6	330	441	200	23%
168 × 5	286	352	206	21%
168 × 8	295	370	208	21%

hammer system, consisting of an indenter (cylindrical with a diameter of 290 mm) and a frame, had a total mass of 430 kg. The drop hammer system's maximum lifting height was 20.6 m. Prior to the lateral impact test, the specimen's ends were constrained by the clamping system (250 mm in each end) to ensure a clamped boundary condition. More impact test setup details can be found in Wang et al. [27].

Fig. 2 depicts the impact force- and mid-span deflection-time histories, while Table 3 summarizes the test results. It's evident from both the figure and table that increasing the thickness of the outer steel tube leads to a considerable rise in peak and plateau impact forces, indicating improved impact resistance. With an increase in impact energy from 12.6 to 16.9 kJ, there is a corresponding increase in peak impact force and maximum/residual deflection, while the plateau impact force remains consistent. The thickness of the inner steel tube and axial force exhibit minimal influence on the impact force- and mid-span deflection-time histories. Additionally, the substitution of NSC with UHPC results in a remarkable reduction in lateral deflections. For further insights into the impact test results, please refer to Wang et al. [27].

2.4. Axial compression test

After the lateral impact test, the impacted specimens were subsequently tested under static axial compression to obtain their residual axial load capacities. For comparisons, two intact specimens were also tested under the static axial compression. Fig. 1(b) shows the setup of axial compression test. The test setup consists of a rigid shaft, bearing plate and hydraulic jack. It is noted that the choice of the static compression test setup was constrained by the laboratory conditions, as the specimen length of 2 m exceeded the maximum allowable height for the compression testing machine. Consequently, the specimens were positioned horizontally for the axial compression tests, with one end of the axial loading device hinged while the other end was clamped. Before initiating the axial compression test, careful placement of the impacted specimen was ensured that the specimen's bending plane aligned with the rotation plane of the axial loading device (i.e., the specimen deflected towards the ground). The specimen ends were smoothed using high strength motor prior to the compression test for avoiding the stress concentration. For data collection, three linear variable differential transformers (LVDTs) were employed to obtain the lateral deflections of the specimens. These LVDTs were installed at intervals of 350 mm, 700 mm, and 1050 mm away from the specimen end, as illustrated in Fig. 1 (c). Load and deformation data were captured using an electronic data logger at 2 s intervals. Displacement-controlled manner was adopted to compress the column with a loading rate of 0.8 mm/min during the compression test, continuing until failure occurred.

2.5. Axial compression test results

Figs. 3 and 4 illustrate the deformation modes of the impacted and intact specimens after the static axial compression, respectively. In general, the tested specimens exhibit more significant residual deflections after the axial compression test, accompanied by local buckling within the impact region for several specimens (Fig. 4(c)). Moreover, for the impacted specimens, the largest residual deflections usually occur at the column's midspans. While for the two intact specimens (Fig. 4), their largest residual deflections occur at the centre right. This difference indicates that the lateral impact clearly affects the specimen's deformation mode. Comparisons of the deformation modes before and after the axial compression are given in Fig. 5, and it can be observed that the

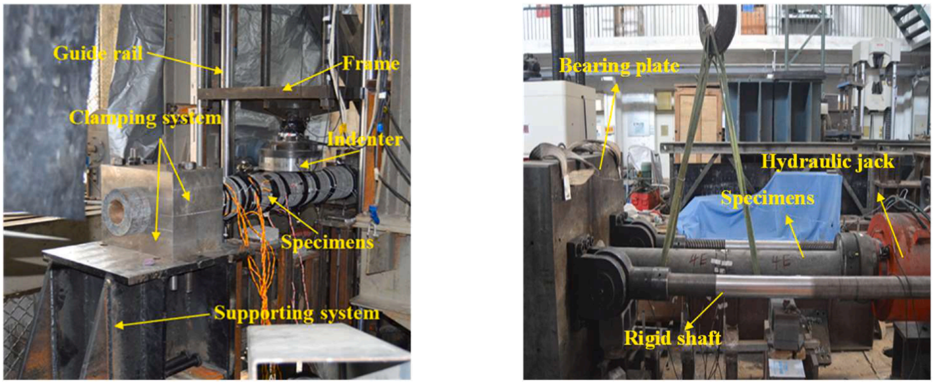

(a) Impact test setup [27]

(b) Axial compression test setup

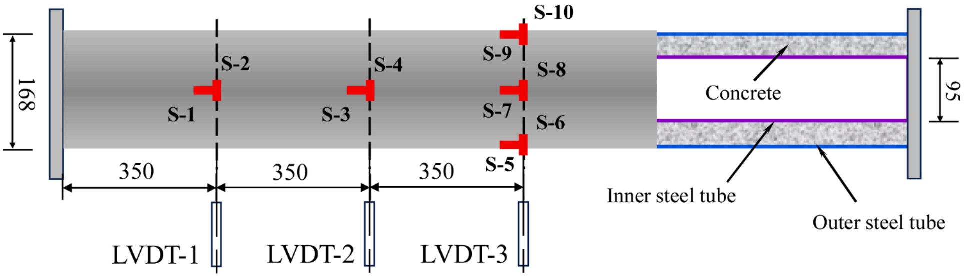

(c) Layout of LVDTs and strain gauges during the axial compression test

Fig. 1. Impact and axial compression test setup (units: mm).

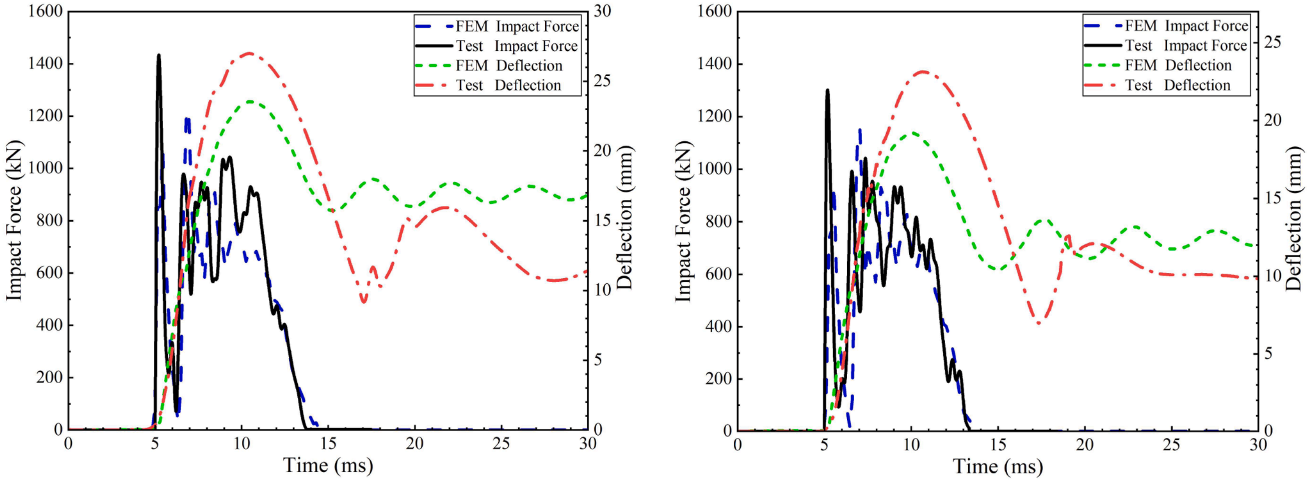

(a) F-U-To5-Ti4-H4

(b) U-To5-Ti4-H3

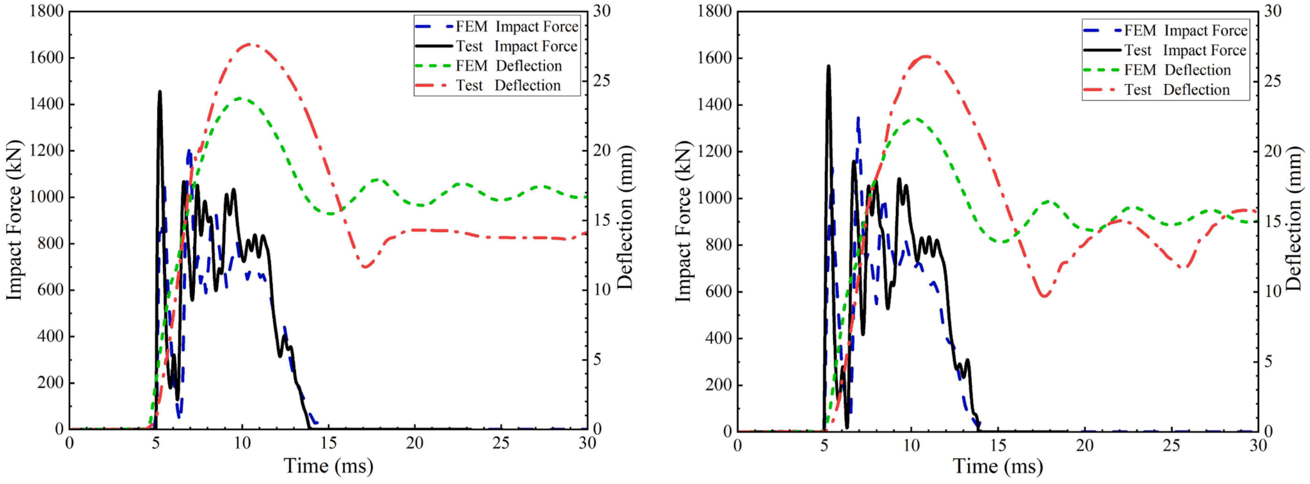

(c) U-To5-Ti4-H4

(d) U-To5-Ti6-H4

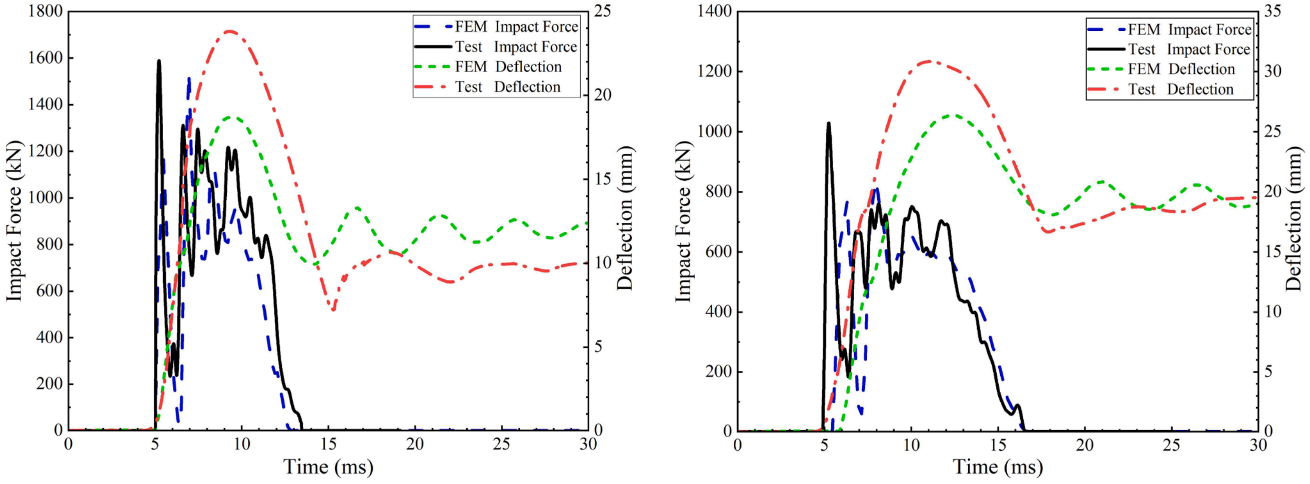

(e) U-To8-Ti4-H4

(f) N-To5-Ti4-H4

Fig. 2. Impact force and mid-span deflection-time histories.

Table 3
Summary of impact and compression test results.

Specimen	F_{max} (kN)	F_p (kN)	t_d (ms)	Δ_{max} (mm)	Δ_u (mm)	F_a (kN)
U-To5-Ti4-H3	1301.8	714.0	8.3	23.1	9.8	1627.8
U-To5-Ti4-H4	1456.6	813.2	8.9	27.6	14.1	1435.3
U-To8-Ti4-H4	1589.1	969.9	8.4	23.8	10.0	2223.3
U-To5-Ti6-H4	1567.3	821.9	8.8	26.8	13.5	1779.1
F-U-To5-Ti4-H4	1434.5	813.3	8.74	27.0	13.4	1655.6
N-To5-Ti4-H4	1029.0	631.6	11.5	30.8	19.1	1494.9
U-To5-Ti4-H0	-	-	-	-	-	2193.2
N-To5-Ti4-H0	-	-	-	-	-	1686.1

Note: F_{max} and F_p indicate the peak and plateau impact forces, respectively; Δ_{max} and Δ_u respectively represent the maximum and residual mid-span deflections; t_d indicates the impact duration; and F_a indicates the axial load capacity.


(a) U-To5-Ti4-H3


(b) U-To5-Ti4-H4


(c) U-To8-Ti4-H4

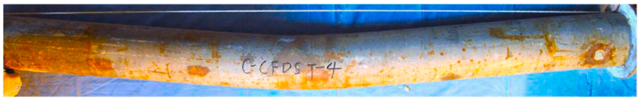
(d) U-To5-Ti6-H4


(e) F-U-To5-Ti4-H4


(f) N-To5-Ti4-H4

Fig. 3. Deformation modes of impacted specimens after the axial compression.

specimen's lateral deflection experienced a noticeable increase after the axial compression.

Fig. 6 illustrates the axial load-deformation behavior of specimens during the axial compression, and the detailed test results are summarized in Table 3. All the specimens exhibit the typical post-peak softening behaviour during the static axial compression, and the lateral deflection experiences more rapid increase than the axial deformation after the peak axial load. As contrast to the intact columns, the impacted specimens have significantly lower axial load capacities and axial stiffnesses. In addition, increasing the thicknesses of two steel tubes can effectively improve the specimens' residual axial load capacities. The specimen's residual axial load capacity can also be increased to a certain extent by applying an axial force during the impact. Moreover, the substitution of NSC with UHPC leads to a substantial increase in both the axial stiffness and residual axial load capacity. It is also noted that the axial stiffness of specimen U-CFDST mutates during the axial compression, which was due to the outer steel tube's local bulking at the column's bottom end, as shown in Fig. 4(c).

3. Numerical simulations

3.1. Finite element modelling

Numerical simulations were conducted using the ANSYS/LS-DYNA software for investigating the impact and post-impact behaviour of UHPC-filled DST columns. The developed numerical model includes the clamping system, drop hammer system, loading plate, and the CFDST column. The 8-node solid hexahedron element was adopted. Moreover, to avoid the element distortion during the calculation, the viscous hourglass was adopted. Given the experimental observations that no


(a) Before the axial compression


(b) After the axial compression

Fig. 5. Deformation modes of Specimen U-To5-Ti4-H3.


(a) U-To5-Ti4



(b) N-To5-Ti4 (c) Local buckling

Fig. 4. Deformation modes of intact specimens after the axial compression.

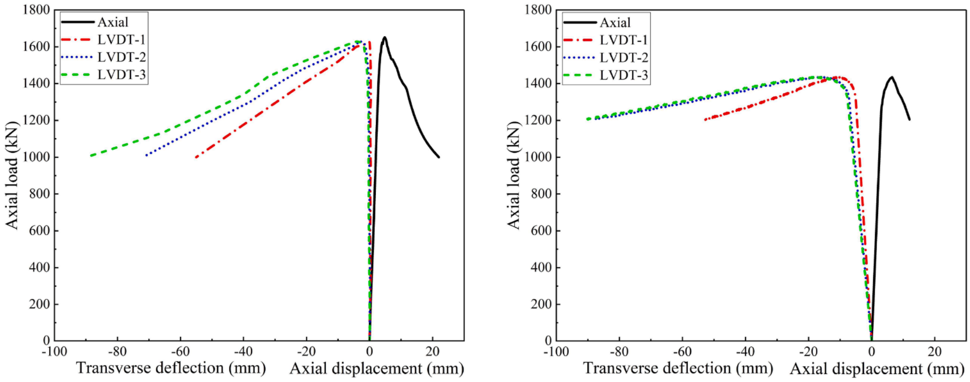

(a) U-To5-Ti4-H3

(b) U-To5-Ti4-H4

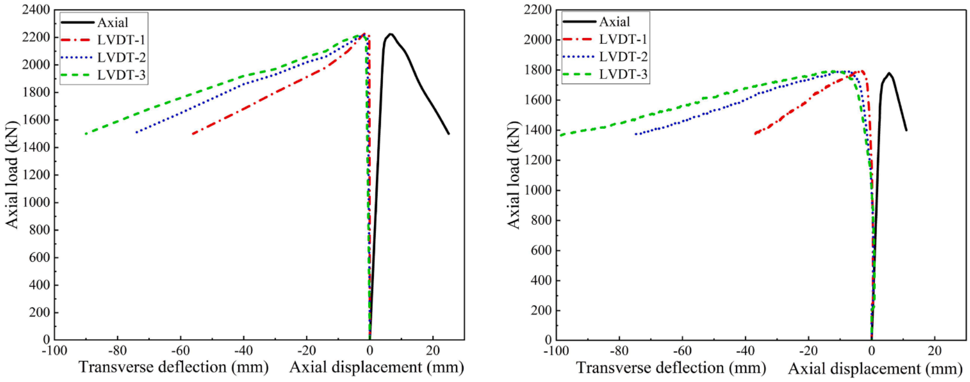

(c) U-To8-Ti4-H4

(d) U-To5-Ti6-H4

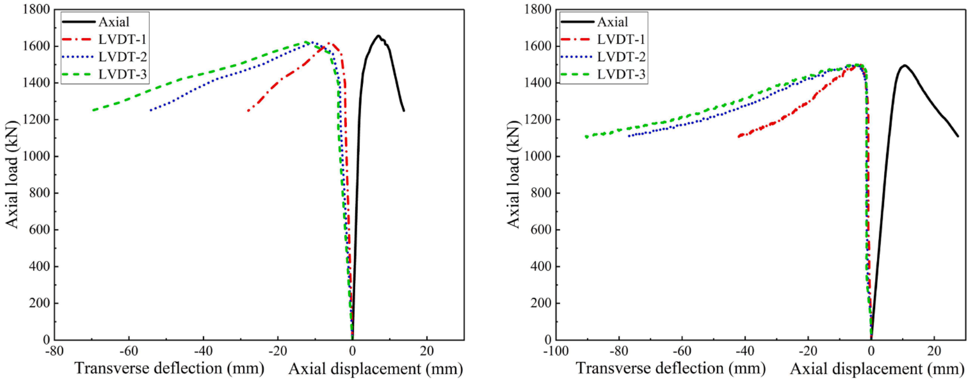

(e) F-U-To5-Ti4-H4

(f) N-To5-Ti4-H4

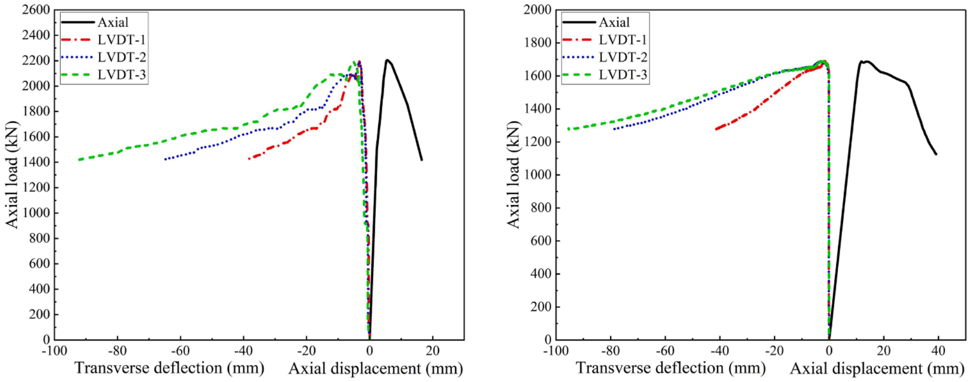

(g) U-To5-Ti4-H0

(h) N-To5-Ti4-H0

Fig. 6. Axial load-deformation behaviors of specimens.

debonding occurred between the concrete and steel tubes during the tests, it was assumed that perfect bond existed between the steel tubes and infilled concrete. The keyword Contact_Automatic_Surface_to_Surface was used to simulate the contact among the column, clamping system, loading plate and the drop hammer system. As suggested, both the static and dynamic friction coefficients were chosen as 0.6 [41].

Fig. 7 shows the developed finite element model. For the infilled concrete and the two steel tubes, the circumferential direction was divided into 80 meshes while the longitudinal direction was divided into 300 meshes, which resulted in an element size of 6.6 mm. Moreover, in order to capture the steel tubes' local buckling behaviour, its thickness direction was divided into three meshes. The numerical model includes a total of 523,986 nodes and 451,296 elements. The mesh sensitivity analysis indicates that by further reducing the element size, the simulation results were similar, but the calculation time was greatly increased.

After the impact simulation stage was completed, only the column and bearing plate are retained, and the full restart method was used to transit the impact simulation to the static simulation. The keyword Stress_Intialization was applied to remain the specimen's stress and strain states at the end of impact simulation as the initial state of the static simulation stage. Moreover, for investigating the residual axial performance of columns, the axial load was applied at the top bearing plate by displacement with a rate of 0.8 mm/min.

3.2. Material models

The continuous surface cap model (CSCM) that combines the continuous damage mechanics with plastic theory was used to simulate the static and dynamic behaviour of concrete [42]. The model includes isotropic constitutive equation, failure and hardening surfaces, as well as the strain rate effect. However, traditional CSCM model is not suitable for the UHPC. Therefore, modifications should be made onto the CSCM model to reflect the complex behaviour of UHPC. Many studies have been carried out to identify the suitable material models for the UHPC. Different constitutive models, such as the K&C, CSCM, and HJC models, were discussed and evaluated [43–45]. Among these models, the CSCM model was found to be capable of capturing the complex dynamic behaviour of UHPC if appropriate modifications can be made [45]. A large number of uniaxial and triaxial material tests of UHPC samples were conducted to calibrate the CSCM model parameters, and these modifications encompass the triaxial material strength, pressure-volumetric change, post-peak softening, and strain rate effects [45]. The detailed parameters of the modified CSCM model for the UHPC are provided in Table 4. Moreover, to avoid the excessive concrete deformation and the calculation overflow, the erosion algorithm was used in this study. It should be noticed that the erosion algorithm has no real physical meaning and the selection of the erosion value should be careful. In this study, the principal strain-based erosion algorithm was adopted, and an erosion value of 0.4 was used after the trials.

The simulation of clamping system, steel frame, and drop hammer system utilized the

Mat_Elastic material model. The keyword Mat_Plastic_Kinematic was used to model the steel tubes. For considering the effect of strain rate, the dynamic increase factor of steel tube (DIF_s) was calculated and is given by [41]:

$$DIF_s = 1 + \left(\frac{\varepsilon_s}{C}\right)^{1/P} \tag{1}$$

where ε_s is the strain rate of the steel tube; C and P are the parameters that are related to material type and strain hardening effect, and the values of C and P were 40.4 s^{-1} and 5, respectively.

3.3. Model validations

Fig. 2 illustrates the comparisons between the collected and predicted impact force- and mid-span deflection-time histories. Generally, the developed numerical model accurately predicts the plateau impact force and duration, albeit underestimating the peak impact force. Several factors contribute to this underestimation. Firstly, the actual contact condition influences the contact stiffness between the column and hammer, thereby affecting the peak impact force. Secondly, impact-induced noises can disrupt the load cell output, leading to inaccuracies in determining the peak impact force. Additionally, Fig. 2 presents the comparisons of experimental and predicted mid-span deflection-time histories. While the overall trends in mid-span deflection are reasonably predicted, the maximum deflections are underestimated. This discrepancy could stem from the factors such as the small interstice between the two steel tubes affecting concrete casting quality, as well as difficulties in evenly distributing steel fibres during the pouring process, and thus results in lower concrete compressive strength. Considering the intricacies of the impact test setup and the simplifications in the numerical simulations, the developed numerical models are deemed reliable in providing reasonable predictions of impact response.

Comparisons between the experimental and predicted deformation modes of the impacted-and-compressed specimen are shown in Fig. 8. Because the deformation modes are similar for all the specimens, only one column's experimental and predicted deformation modes are presented in this study. It is evident from Fig. 8 that accurate lateral deflection prediction can be achieved. Comparisons of experimental and

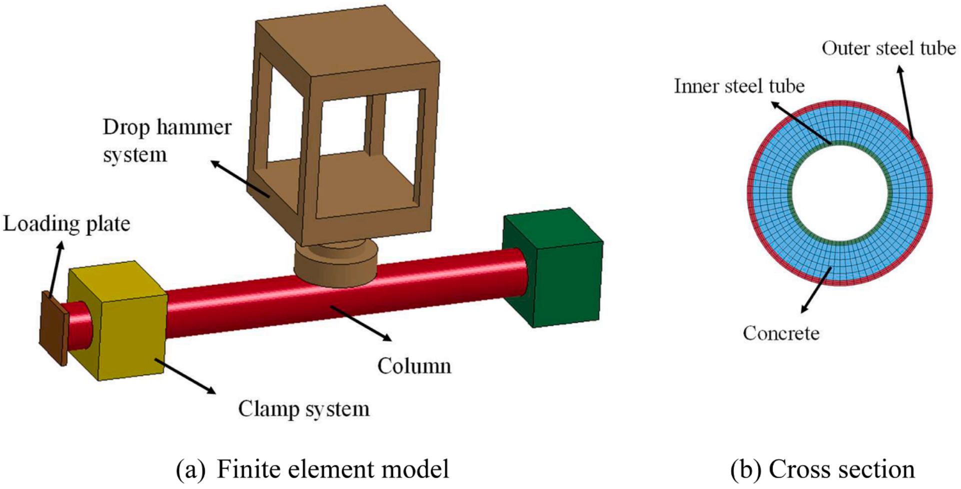

(a) Finite element model (b) Cross section

Fig. 7. Developed numerical model.

Table 4
Material parameters for UHPC (f_{co}=136MPa).

Parameter	Magnitude	Parameter	Magnitude	Parameter	Magnitude	Parameter	Magnitude
$RO\ (kg/m^3)$	2600	$NPLOT$	1	$INCRE$	0	$IRATE$	1
$ERODE$	1.3	$RECOV$	0	$ITRETRC$	0	$PRED$	0
$G(Pa)$	1.800E+10	$K(Pa)$	2.500E+10	N_H	0	C_H	0
$\alpha(Pa)$	4.590E+7	θ	0.2873	$\lambda(Pa)$	3.65E+7	$\beta(Pa^{-1})$	1.260E-8
α_1	1	$\theta_1\,(Pa^{-1})$	0	λ_1	0.4226	$\beta_1\,(Pa^{-1})$	1.277E-9
α_2	1	$\theta_2\,(Pa^{-1})$	0	λ_2	0.5	$\beta_2\,(Pa^{-1})$	1.277E-9
R	6	$X_0(Pa)$	6.000E+8	W	0.050		
D_1	6.000E-10	$D_2\,(Pa^{-2})$	0				
B	100	$GFC(N/m)$	1.000E+4	D	0.1	$GFT(N/m)$	1000
$GFS(N/m)$	1000	$pwrc$	5	$pwrt$	1	$pmod$	0
η_{0c}	1.830E-4	N_C	0.504	η_{0t}	1.760E-5	N_t	0.56
$overc(Pa)$	1.050E+8	$overt(Pa)$	7.760E+6	$Srate$	1	$repow$	1

predicted axial force-deformation behaviour are shown in Fig. 9. Note that only the UHPC-filled DST columns were used for the validations. In general, the prediction results match well with the experimental data, and the residual axial load capacities of most specimens can be accurately predicted. Specifically, the numerical model underestimates the axial load capacity for specimen “U-To8-Ti4-H4”. Compared to other specimens, specimen “U-To8-Ti4-H4” had an outer steel tube thickness of 8 mm, resulting in a very large confinement pressure of 30.1 MPa. Therefore, it is suggested that the confinement effect might be underestimated in the modified CSCM model. In fact, the accuracy of modified CSCM model depends on the collected UHPC database. If the triaxial compression test data of UHPC were inadequate, the accuracy of modified CSCM model might be less for the confined UHPC. Moreover, it is noteworthy that the predicted axial stiffnesses are larger than the experimental values in some cases. This discrepancy can be attributed to the fact that the LVDT readings encompass not only the specimen’s axial deformation, but also include the deformation of the loading machine, as well as the deformations caused by uneven specimen ends, among other factors [46]. To sum up, accurate simulation of the column’s post-impact behaviour is acknowledged as challenging, given its reliance on the accuracies of both the impact simulation and the subsequent static simulation [28]. Despite these challenges, the developed numerical models are deemed reliable and were utilized for further investigations.

3.4. Impact resistant mechanism

The Chinese standard suggested the design equations for the impact resistant design of CFDST columns, in which the equations were derived based on the database of mid-height impacted CFDST columns [47]. In practice, the ship or vehicle collisions usually occur at the column’s lower part. Therefore, the impact behaviour of CFDST columns at different impact locations was investigated in this chapter. For simplification, the bottom end of CFDST column was fully constrained, while the top end was fully constrained except for the longitudinal direction. A rigid body with a size of 0.2 m × 0.5 m × 0.5 m was used to represent the impacting component, as shown in Fig. 10(a). The mass and impact velocity of the impacting component were 1000 kg and 10 m/s (impact energy 50 kJ), respectively. The detailed model parameters are provided in Table 5.

To investigate the impact location’s effect on the impact behaviour of CFDST column, two different impact locations, the mid-height and 1/4 height (from bottom to top), were selected. Fig. 10(b) shows the column’s impact force- and deflection-time histories of two selected points, in which Point A is the collision centre at the front side, while Point B locates at the rear side. It is apparent from Fig. 10(b) that for the mid-height impact, the impact force-time history is a typical three-stage curve, including a peak ascending stage, followed by a plateau stage and an unloading stage. While for the 1/4 height impact, the peak impact force is visibly higher than that of the mid-height impact (increases rapidly from 2263 kN to 3048 kN). Moreover, the duration of plateau impact force stage is very short as compared to that of mid-height impact. In addition, the lateral deflection-time histories also differ remarkably by changing the impact location. By changing the impact location from the mid-height to the 1/4 height, both the lateral deflections at the front and rear sides decrease greatly. Specifically, the lateral deflection difference between the Points A and B becomes more signficant for the 1/4 height impact, while the lateral deflection difference is less significant for the mid-height impact. The primary reason for this phenomenon lies in the constraint imposed by the bottom column end, which hinders the development of global deflection. Consequently, a larger proportion of impact energy was disipitted within the impact region, resulting in a more severe localized deflection. Overall, when the impact height becomes closer to the column bottom, the global deflection becomes smaller while the localized deflection of the impacted section increases.

For the 1/4 height impact scenario, the lateral deflection distributions throughout the column height are shown in Fig. 11. In addition to Points A and B, a number of points with an interval of 0.3 m were selected from both the front and rear sides. As can be seen from Fig. 11, the lateral deflections at the front and rear sides are very close at the non-impact regions, while there is a large lateral deflection difference between the front and rear sides at the impact region. This remarkable difference is due to the localized deformation within the impact region.

(a) Experimental deformation mode

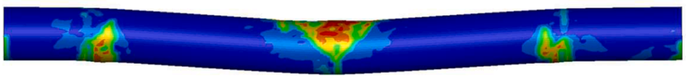

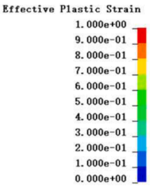

(b) Predicted deformation mode

Fig. 8. Comparisons between the experimental and predicted deformation modes of specimen U-To5-Ti6-H4.

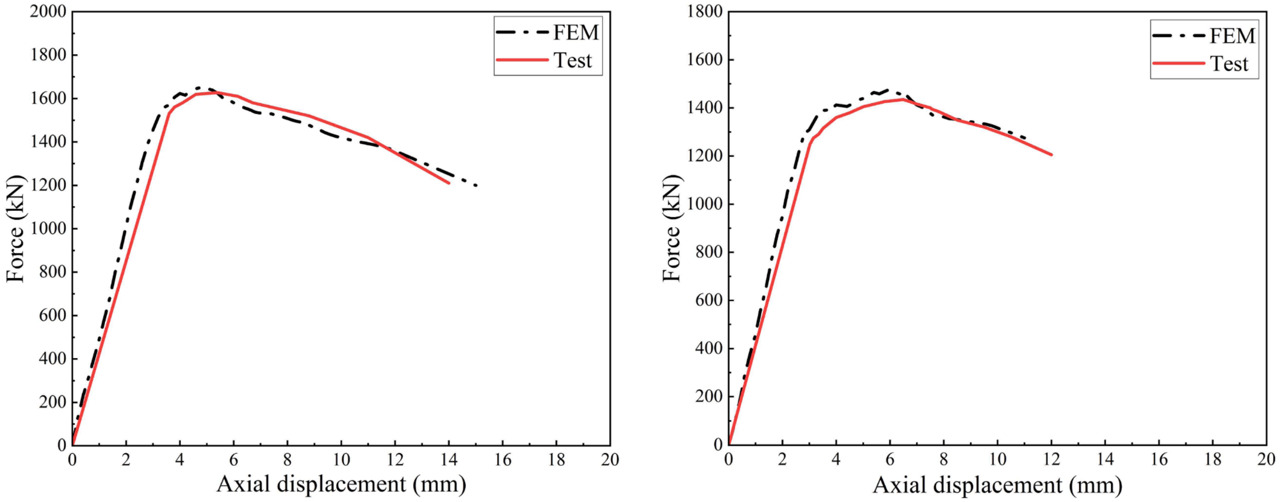

(a) U-To5-Ti4-H3

(b) U-To5-Ti4-H4

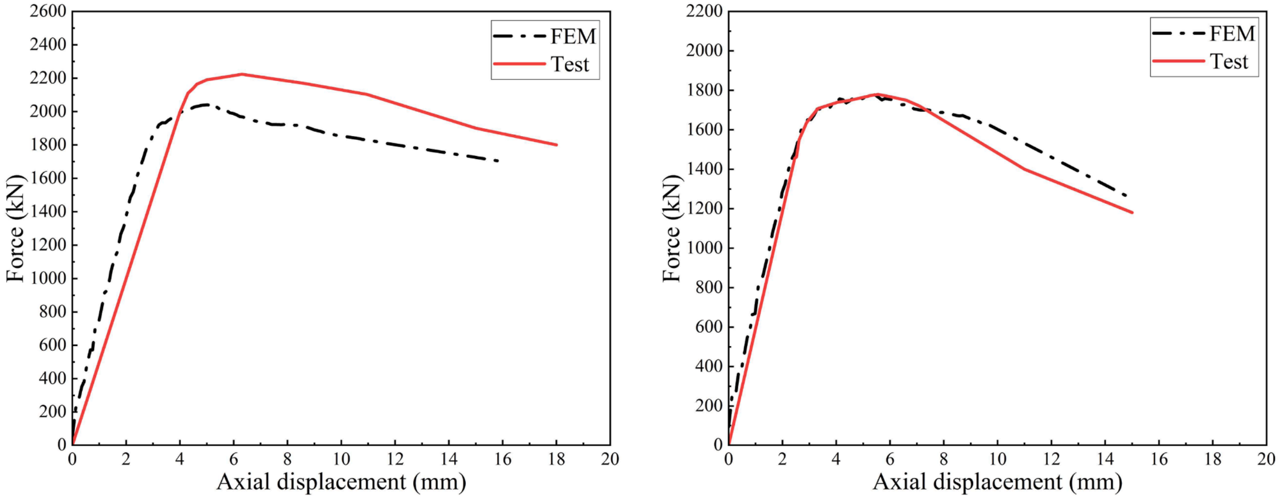

(c) U-To8-Ti4-H4

(d) U-To5-Ti6-H4

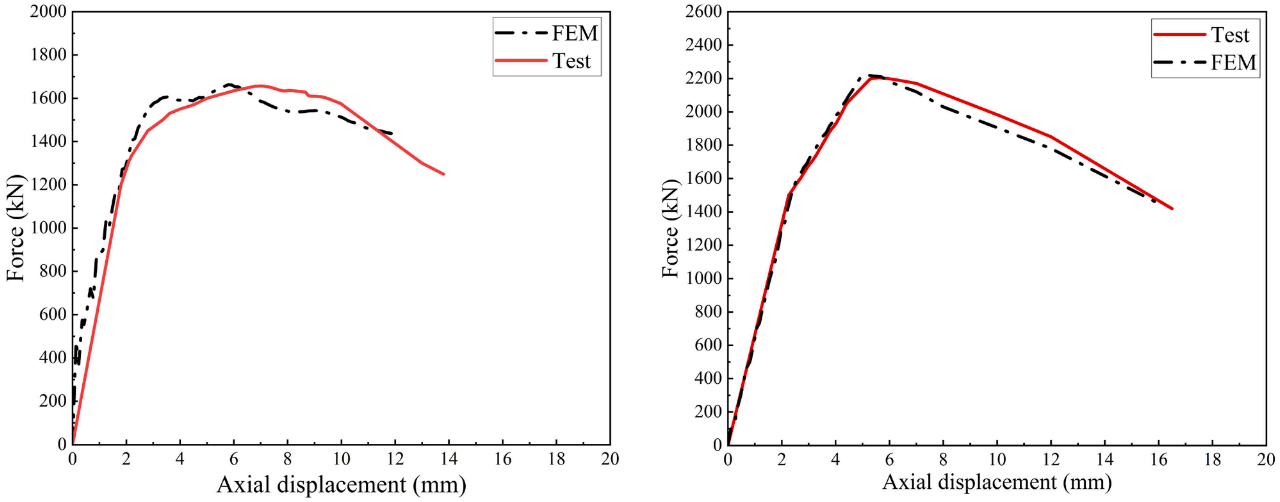

(e) F-U-To5-Ti4-H4

(f) U-To5-Ti4-H0

Fig. 9. Comparisons between the experimental and predicted axial load-deformation behaviors.

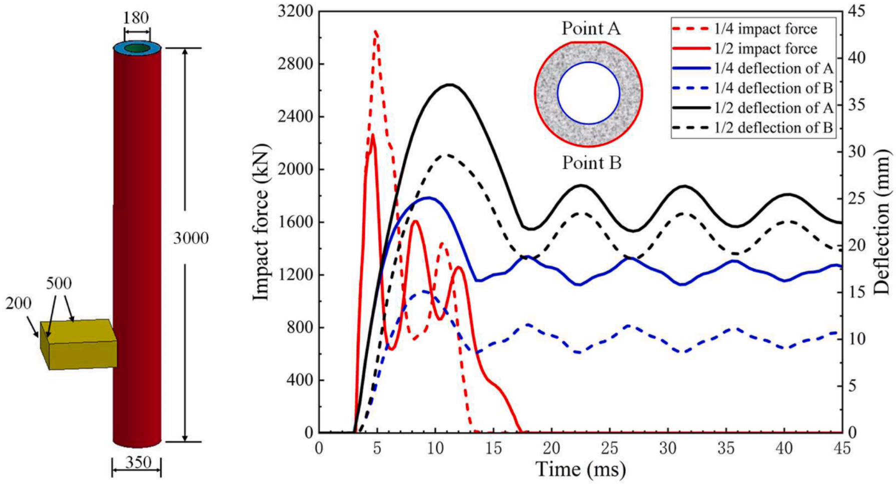

(a) Finite element model (b) Impact force- and lateral deflection-time histories at different impact heights

Fig. 10. Impact resistant mechanisms at different impact heights (units: mm).

Table 5
Finite element model size table.

H (mm)	t_1 (mm)	t_2 (mm)	*D* (mm)	*d* (mm)	f_{y1} (MPa)	f_{y2} (MPa)	f_c (MPa)	*α*
3000	6	4	350	180	345	345	135	0.5

Note: *H* indicates the height of specimen; t_1 and t_2 indicate the thicknesses of outer and inner steel tube, respectively; *D* and *d* indicate the outer and inner diameters of specimen, respectively; f_{y1} and f_{y2} indicate yield stresses of outer and inner steel tube, respectively; f_c indicates the concrete strength; and *α* indicates the axial load ratio.

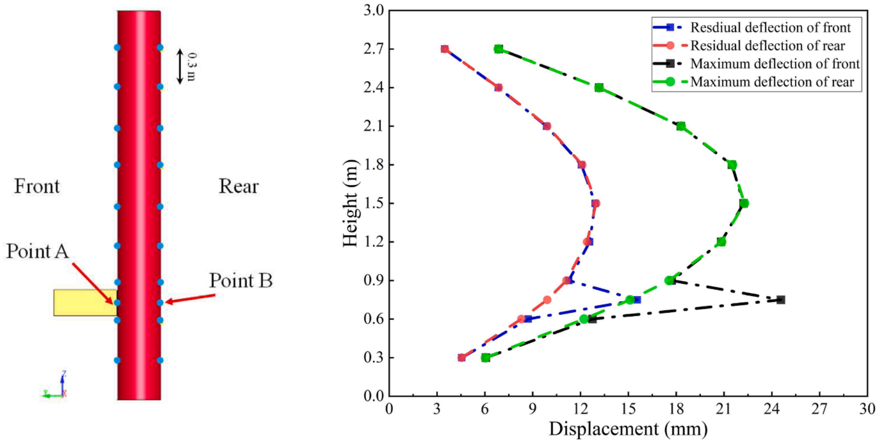

(a) Selected points (b) Maximum and residual deflection distributions

Fig. 11. Distributions of maximum and residual deflections throughout the column height.

Therefore, for the hollow section CFDST column, the reduced local stiffness may result in significant local deflection and this cannot be ignored during the impact and post-impact analysis. Moreover, except for the impact region, the column's mid-height still undergoes the largest maximum and residual lateral deflections.

The deformation and damage modes of columns under different impact heights are shown in Fig. 12. After the static axial compression, the concrete damage and the deflection experience noticeable increases. In addition, the concrete damage of the impact section is also provided. The concrete damage at the rear side is more severe under the mid-height impact. It should also be noted that under the 1/4 height impact, the concrete damage manifests at a 45° angle on both sides of the upper section, indicating a possible occurrence of concrete shear failure. Therefore, with the impact location closer to the column bottom, the local deflection and the likelihood of concrete shear failure will dominate the impact response of CFDST column. Moreover, the damage modes of steel tubes are also shown in Fig. 12. Under the mid-height impact, the damage of outer and inner steel tubes becomes more severe.

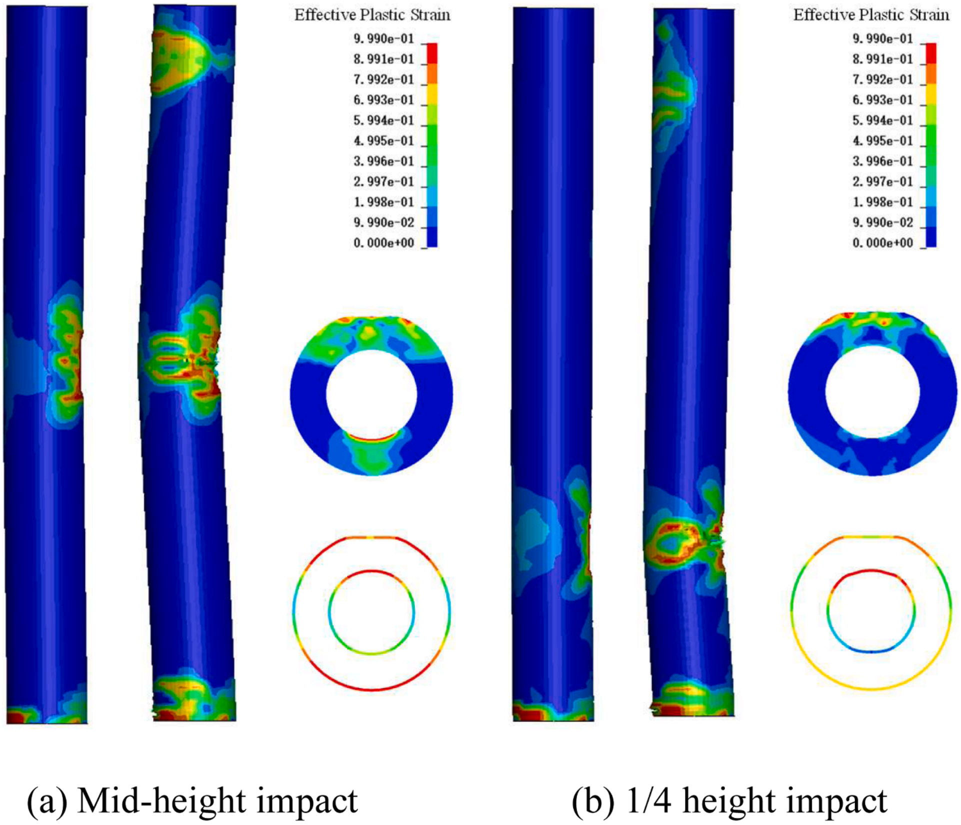

(a) Mid-height impact

(b) 1/4 height impact

Fig. 12. Damage modes under different impact heights (Left: before compression, right: after compression).

The internal energy variations of three components (outer steel tube, inner steel tube, and concrete) under different impact locations are presented in Fig. 13. Under the mid-height impact, the outer steel tube absorbs the most kinetic energy, followed by the concrete and inner steel tube. However, under the 1/4 height impact, the concrete absorbs the most kinetic energy, followed by the outer and inner steel tubes. When the impact location is close to the column end, more impact energy is dissipated in the impact region, and thus the concrete is more likely to exhibit shear failure. Therefore, during the strengthening and retrofitting schemes, external wrapping of steel strips and FRP jacket can be adopted to improve the column's shear performance. In addition, the void can be partially filled with soft/rigid foams to prevent excessive local deformation to further improve the impact resistant capacity.

The residual axial load capacities of UHPC-filled DST columns with different impact locations and impact energies are presented in Fig. 14. The impact energies are ranged from 8 kJ to 98 kJ. It can be seen from Fig. 14 that, when the impact energy is low, the column under the 1/4 height impact has larger residual axial load capacity. However, with a large impact energy, the column under the mid-height impact has larger residual axial load capacity. With a low impact energy, the column's local deflection is small for both impact scenarios. Therefore, the local deflection has less influence on the residual axial loading capacity. With

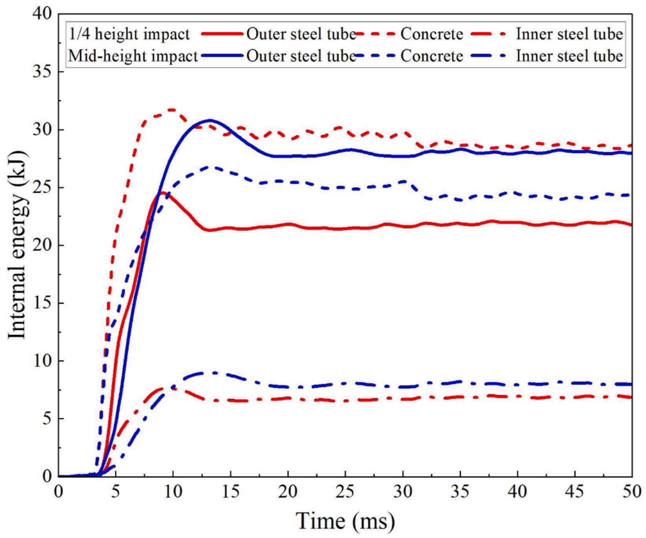

Fig. 13. Internal energy variations.

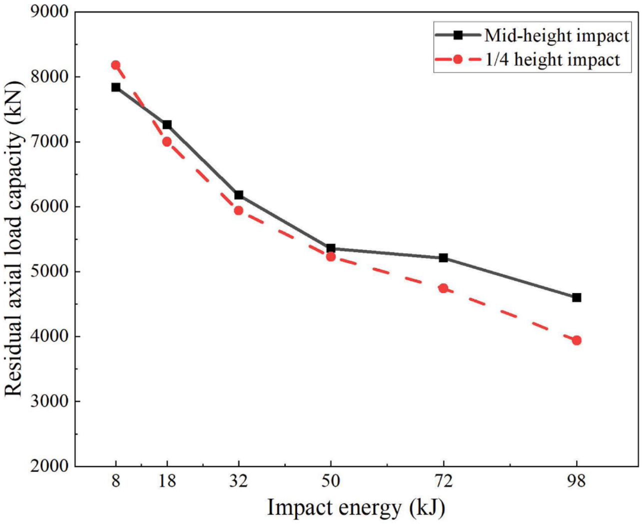

Fig. 14. Residual axial load capacities under different impact energies.

a larger impact energy, the column's local deflection becomes more significant. In this case, the local deflection plays a more important role in decreasing the residual axial loading capacity.

4. Selections of damage indexes for impacted CFDST column

In this study, the damage level (*DL*) of impacted UHPC-filled DST columns can be quantitatively described by:

$$DL = 1 - P_r/P_n \tag{2}$$

where P_n and P_r indicate the axial load capacities of the non-impacted and impacted columns, respectively.

It should be acknowledged that accurate measurement of the residual axial load capacity of impacted concrete column is challenging in practise. Li et al. [48] and Cui et al. [49] introduced a deflection-based damage index for predicting the damage of blasted RC columns. They found that the damage level of RC columns could be adequately forecasted by utilizing the ratio of mid-height deflection to column height. However, these studies only accounted for the global lateral deflection when predicting the damage of RC columns. Nevertheless, for the impacted CFDST columns, there is a non-negligible localized deflection due to the presence of a void, which can further deteriorate its residual performance [50]. Until now, rational damage indexes for the damage evaluation of hollow concrete columns are still not available. Consequently, damage indexes were proposed to evaluate the impact damage of CFDST columns, in which both the global and localized deflections can be considered.

For the CFDST column, the ratio of mid-height deflection to column height can be used to reflect the influence of global deflection on the column's damage. Both the maximum and residual deflections can be used, and the mid-height deflection-based damage indexes are given by:

$$X_1 = \frac{\delta_B}{L} \tag{3}$$

$$R_1 = \frac{\omega_B}{L} \tag{4}$$

where X_1 and R_1 indicate the maximum and residual mid-height deflections to column height ratios, respectively; L indicates the column height; δ_B indicates the maximum mid-height deflection; and ω_B indicates the residual mid-height deflection.

Moreover, the ratio of lateral deflection difference between Points A and B to the column diameter was used to reflect the influence of local deflection on the column's damage (Fig. 10), and the local deflection-based damage indexes can be given by:

$$X_2 = \frac{\delta_A - \delta_B}{D} \tag{5}$$

$$R_2 = \frac{\omega_A - \omega_B}{D} \tag{6}$$

where X_2 and R_2 indicate the maximum and residual local deflections to the column diameter ratios, respectively; D is the column's outer diameter; δ_A and δ_B indicate the maximum deflections at Points A and B, respectively; ω_A and ω_B indicate the residual deflections at Points A and B, respectively.

The selections of damage indexes should consider both the prediction accuracies and the availability of damage indexes. If the prediction accuracies are similar, the residual deflection-based damage indexes should be used since the residual deflections can be easily measured after the impact. The prediction accuracies using different damage indexes were evaluated by using a large number of simulation data. 100 groups of samples with 1/4 height impact scenario were modelled to obtain the values of residual axial load capacities and different damage indexes, and the selected column design variables and impact parameters are given in Table 6. The nonlinear relationships between the damage level (*DL*) and the four damage indexes (*R_1, R_2, X_1* and *X_2*) are shown in Fig. 15, in which the fitting curves between the damage index and (*DL*) are given. In addition, the 95 % confidence intervals of fitting curves and 95 % prediction blanks of prediction points are also provided. The prediction accuracy is assessed by the adjusted R-Square. As can be seen from Fig. 15, when the cubic polynomial was used for the curve fitting, the fitting determination coefficients are greater than 0.9 for all cases. Therefore, strong correlations exist between the damage indexes and the *DL*: the larger the global/residual deflection, the more severe the column damage. The fitting determination coefficients are 0.922 and 0.962, respectively, by using the maximum deflection-based damage indexs X_1 and X_2. Similarly, the fitting determination coefficients by using the residual deflection-based damage indexes R_1 and R_2 are also similar (0.917 and 0.956). Therefore, the use of residual deflection-based damage indexes (R_1, R_2) can achieve comparable prediction accuracies as compared to the use of maximum deflection-based damage indexes (X_1, X_2). Due to this, the residual deflection-based damage indexes, R_1 and R_2, were selected for the damage evaluation of impacted CFDST columns in the following studies.

Moreover, another 200 groups of samples with the 1/3 and 1/5 height impact scenarios were modelled, with 100 groups of samples for each impact height. The generated database was used to assess the relationship between the damage index R_1 and *DL*. The nonlinear relationships between the damage index R_1 and *DL* at different impact heights are shown in Fig. 16. When the impact location moves from the 1/3 height to the 1/5 height, the fitting determination coefficient decreases from 0.961 to 0.891. This indicates that the closer the impact location to the column bottom, the lower the prediction accuracy of solely using damage index R_1. Therefore, only consideration of global deflection-based damage index R_1 is unable to accurately predict the impact damage of hollow concrete columns, and it is necessary to combine the global deflection-based damage index (R_1) and local deflection-based damage index (R_2) for the damage predictions.

5. Damage assessment using machine learning techniques

Several studies proposed the empirical formulae for the damage assessment of impacted concrete columns based on the collected database. Nevertheless, owing to the complex mechanisms, prediction formulae using traditional regression analysis method are not able to accurately predict the damage of impacted concrete columns [37]. Therefore, machine learning techniques were used to develop the damage prediction models for the impacted UHPC-filled DST columns.

Table 6
Input parameters and the value ranges.

Parameter	unit	Value range
H	mm	2000, 3000, 4000
t_1	mm	5, 6, 8, 10
t_2	mm	3, 4, 5, 7
D	mm	200, 350, 500
d	mm	100, 130, 180, 230, 280, 330
f_{y1}	MPa	235, 345, 390, 420
f_{y2}	MPa	235, 345, 390, 420
f_c	MPa	120, 135, 150
m	kg	300~3000
v	m/s	4~30
IL		1/5, 1/4, 1/3
α		0.1, 0.2, 0.3

Note: H indicates the height of specimen; t_1 and t_2 indicate the thickness of outer and inner steel tubes, respectively; D and d indicate the outer and inner diameters of specimen, respectively; f_{y1} and f_{y2} indicate yield strengths of outer and inner steel tubes, respectively; f_c indicates the concrete strength; m and v indicate the mass and velocity of impact hammer, respectively; IL indicates the ratio of impact height to column height (from bottom to top); and α indicates the axial load ratio.

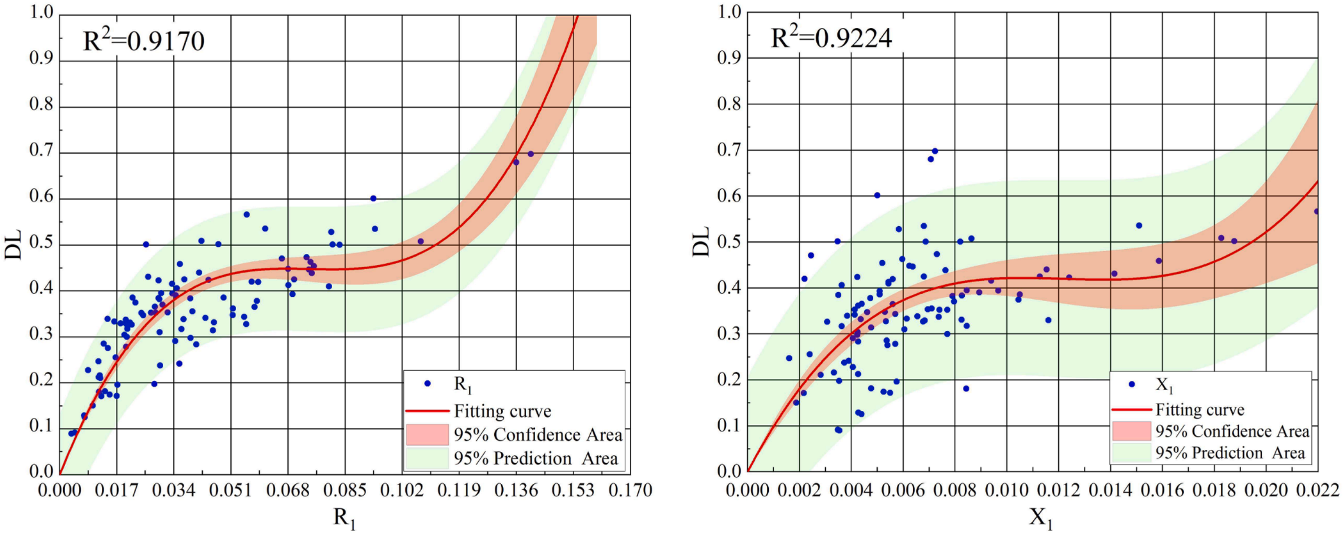

(a) Damage index R_1 (b) Damage index X_1

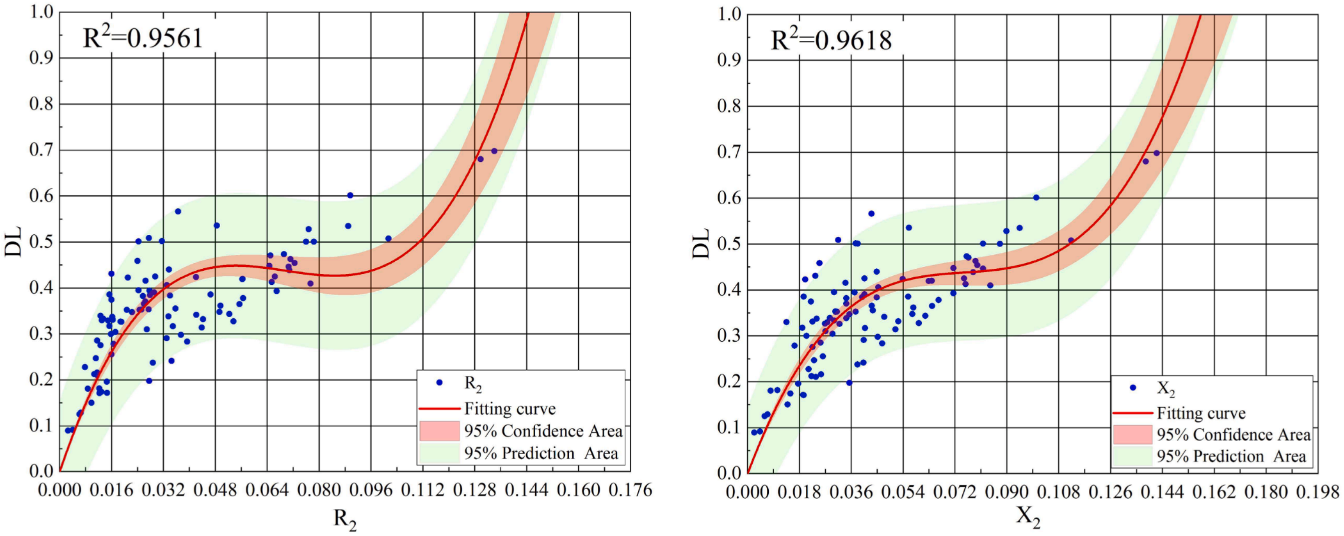

(c) Damage index R_2 (d) Damage index X_2

Fig. 15. Nonlinear relationships between the damage indexes and *DL*.

5.1. Model training and testing

A total of 500 groups of samples were modelled as the sample library, taking into consideration 12 parameters that may affect the residual performance of impacted CFDST columns. The value ranges of these parameters are shown in Table 6. During the process of establishing machine learning models, the datasets were divided into training and test sets, in which the training set was used to train the model, and the test set was used to evaluate the model's prediction accuracy. In this study, the proportions of training and test sets were 70 % and 30 %, respectively, with the division being random.

Two types of machine learning-based models were established. Type I model was used for the impact resistant design, utilizing the column design variables and impact parameters as the inputs. Type II model was used for rapid damage evaluation after the impact, using the column design variables and two damage indexes R_1 and R_2 as the inputs. Three machine learning methods, namely Gaussian process regression (GPR), support vector machine (SVM) and least square boosting (LSBoost), were used to train and validate the machine learning models.

Moreover, in order to optimize the model's hyperparameters, Bayesian optimization was applied to the three machine learning methods using 100 iterations and 5-fold cross-validation. Fig. 17 displays the flowchart for the machine learning models. To assess the model accuracy, two statistical metrics, namely the coefficient of determination (R^2) and the root mean square error (*RMSE*), were employed. The formulas for R^2 and *RMSE* are provided below:

$$R^2 = 1 - \frac{\sum_{i=1}^{n}(Y_i - \widehat{Y}_i)}{\sum_{i=1}^{n}(Y_i - \overline{Y}_i)} \tag{7}$$

$$RMSE = \sqrt{\frac{1}{n}\sum_{i=1}^{n}(Y_i - \widehat{Y}_i)^2} \tag{8}$$

where n is the number of samples; Y_i is the actual value, $\widehat{Y}_i$ is the predicted value, and $\overline{Y_i}$ is the average of the actual values for all samples.

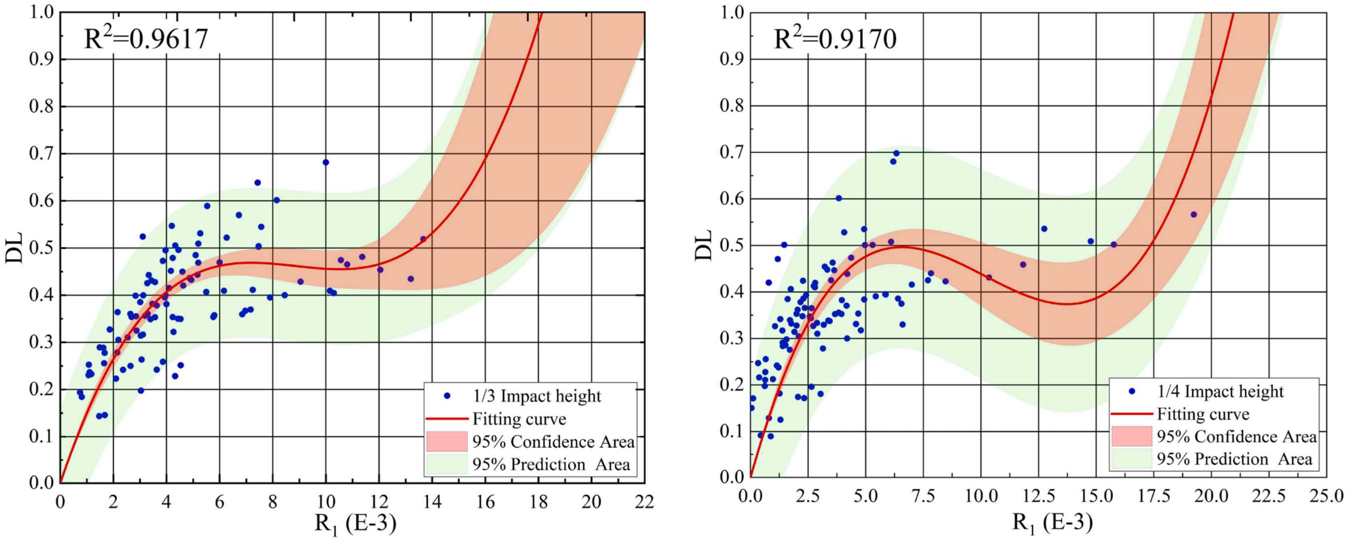

(a) 1/3 height

(b) 1/4 height

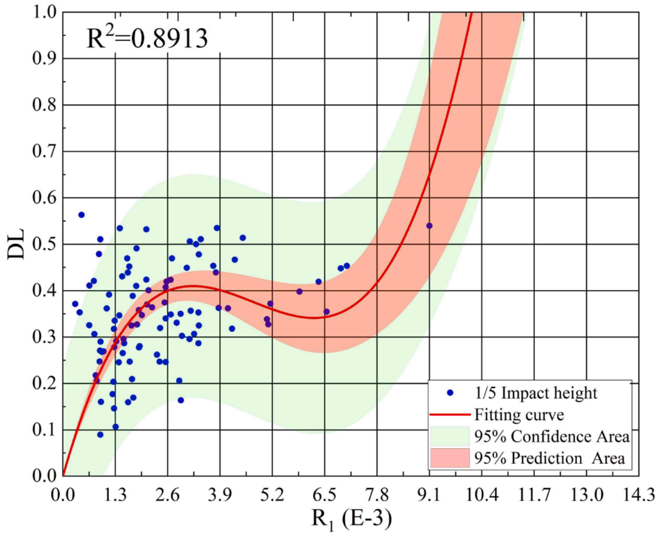

(c) 1/5 height

Fig. 16. Nonlinear relationships between the damage index R_1 and *DL* at different impact heights.

5.2. Performance evaluations

The performance indicators for the machine learning models are shown in Fig. 18. The R^2 values are greater than 0.9 for all the models, and the *RMSE* values are lower than 0.036. This indicates that the three machine learning methods are able to provide accurate predictions for both the Type I and Type II models. Additionally, for the Type II models that used the two damage indexes (R_1 and R_2) as the input parameters, even higher prediction accuracies can be achieved than the Type I models.

Fig. 19 depicts the prediction accuracies of the machine learning models on the test set. It's apparent from the figure that the majority of prediction errors are within a 10 % range, with all prediction errors falling within a 25 % range. This indicates that the three machine learning methods are effective in predicting the damage of impacted UHPC-filled DST columns. It's worth explaining that during the generation of the sample library, the UHPC-filled DST columns with residual axial load capacities less than 30 % of their original axial load capacities were not included in the database. These columns' damage was considered severe enough to be intuitively assessed after lateral impacts, making post-impact retrofitting unnecessary.

Fig. 20 shows the prediction residuals of the machine learning models. It can be seen that the prediction accuracies of Type II models are better than that of Type I models. Meanwhile, the GPR method outperforms the other two machine learning methods for both types of models. Therefore, the two types of machine learning models using the GPR method were analysed and explained in further details.

5.3. Model interpretations

In this study, the Shapley Additive Interpretation (SHAP) method, a model-independent game theory approach proposed by Lundberg and Lee [51], was used to explain the machine learning models using the GPR method. The SHAP method quantifies the contribution of each input variable to a single prediction. Fig. 21 shows the feature importance of the GPR-based machine learning models. The higher the feature

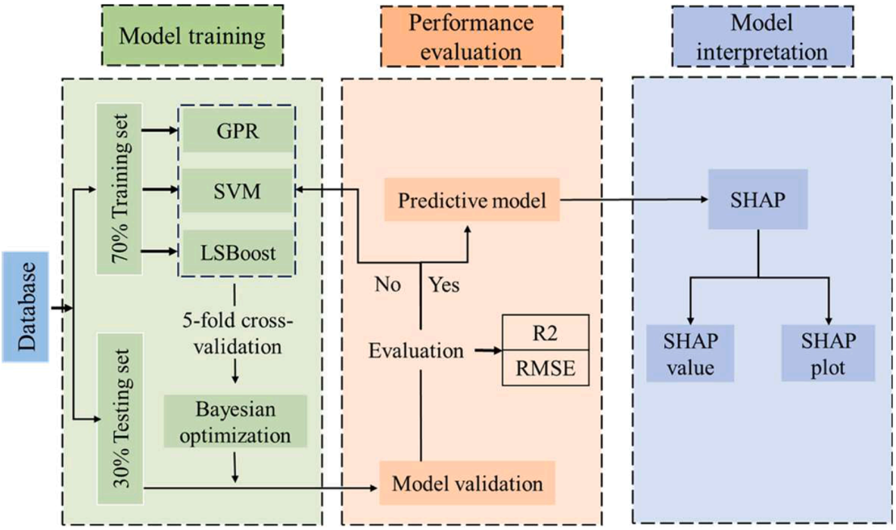

Fig. 17. Machine learning flowchart.

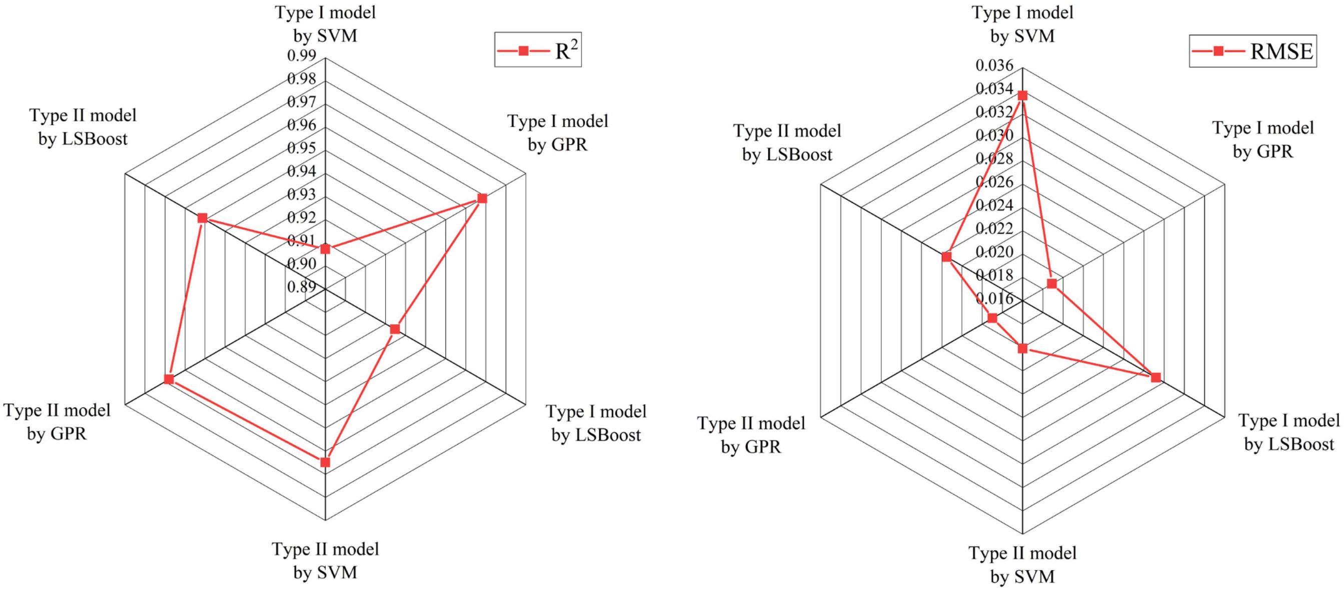

(a) R^2

(b) $RMSE$

Fig. 18. Performance indicators for the machine learning models.

importance value, the more significant the influence of the input variable on the residual bearing coefficient. As evident in Fig. 21, for the Type I model, the impact velocity (v), the impact mass (m) and the column's outer diameter (D) are the variables with the greatest influences on the residual bearing coefficient. Comparably, other variables have moderate influences on the residual bearing coefficient. For the Type II model, the two damage indexes (R_1, R_2) and the column's outer diameter (D) have the greatest influences on the residual load coefficient, followed by other design variables. This observation indicates that the proposed two damage indexes (R_1, R_2) can effectively reflect the damage of impacted hollow CFDST columns.

To determine the parameters' positive or negative impact on the predictions, the SHAP summary diagrams of the two GPR-based machine learning models are presented in Fig. 22. Each row in the figure represents an input variable, sorted from top to bottom based on its importance, with horizontal coordinates representing the SHAP values. The depth of colour indicates the value of input variable values from low to high. As evident in Fig. 22 (a), the residual bearing coefficient of columns decrease while the impact velocity (v) and impact mass (m) increase, indicating these two parameters have negative effects on the residual performance of CFDST column. Moreover, the outer diameter (D) has a positive influence on the residual bearing coefficient, while the inner diameter (d) has a negative effect. Both the outer and inner steel tubes' yield strengths (f_{y1}, f_{y2}) have positive effects on the residual bearing coefficient. As evident in Fig. 22 (b), both the two damage indexes (R_1, R_2) have the higheset negative effects on the residual bearing coefficient. However, for the Type II model, the outer diameter (D) has the negative effect, which may be due to the input of damage index R_2: with the identical R_2 value, the larger column outer diameter means the more severe local deflection, which can negatively affect the residual performance of CFDST columns.

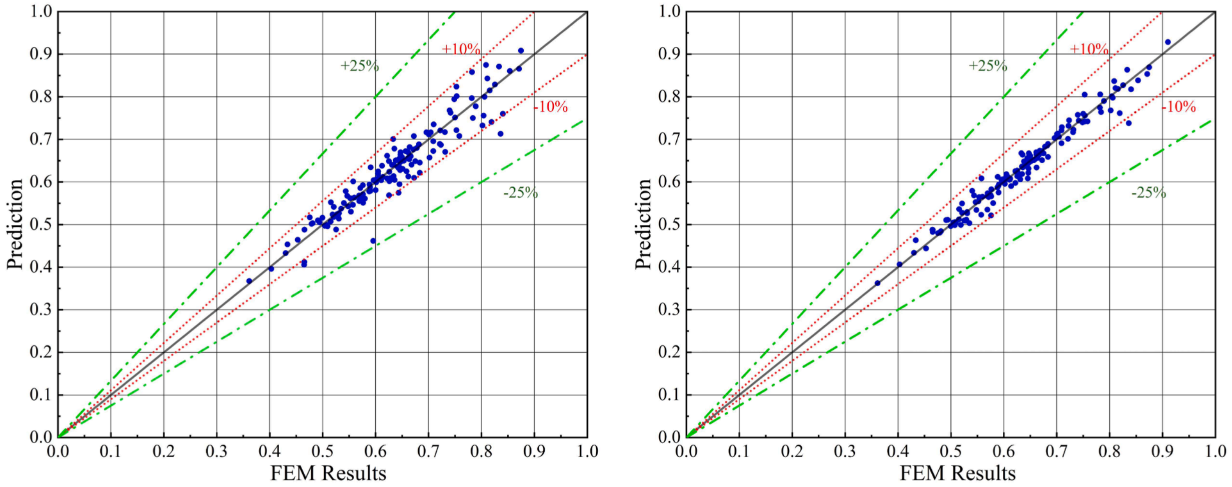

(a) Type I Model: SVM

(b) Type I Model: GPR

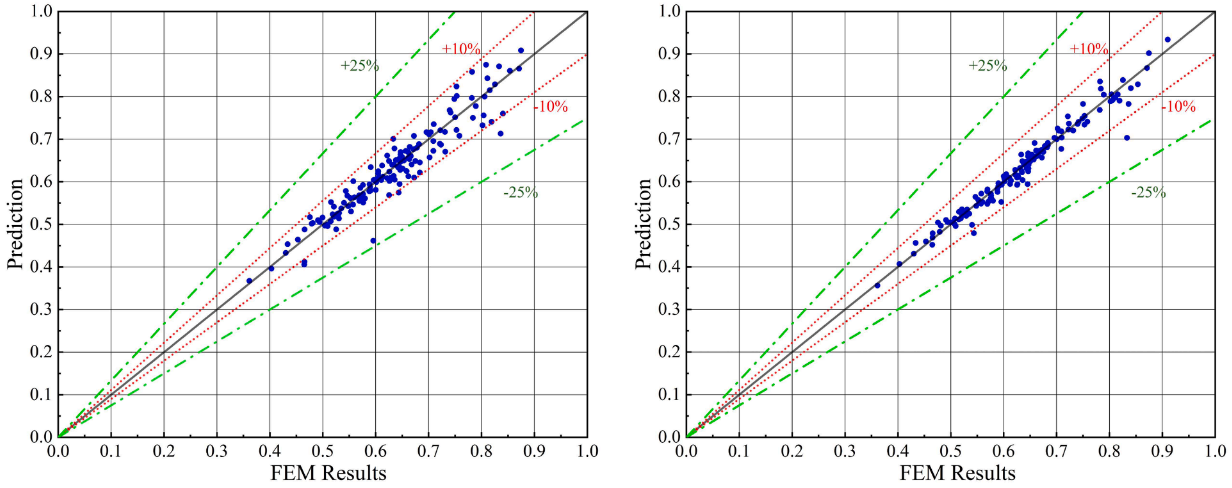

(c) Type I Model: LSBoost

(d) Type II Model: SVM

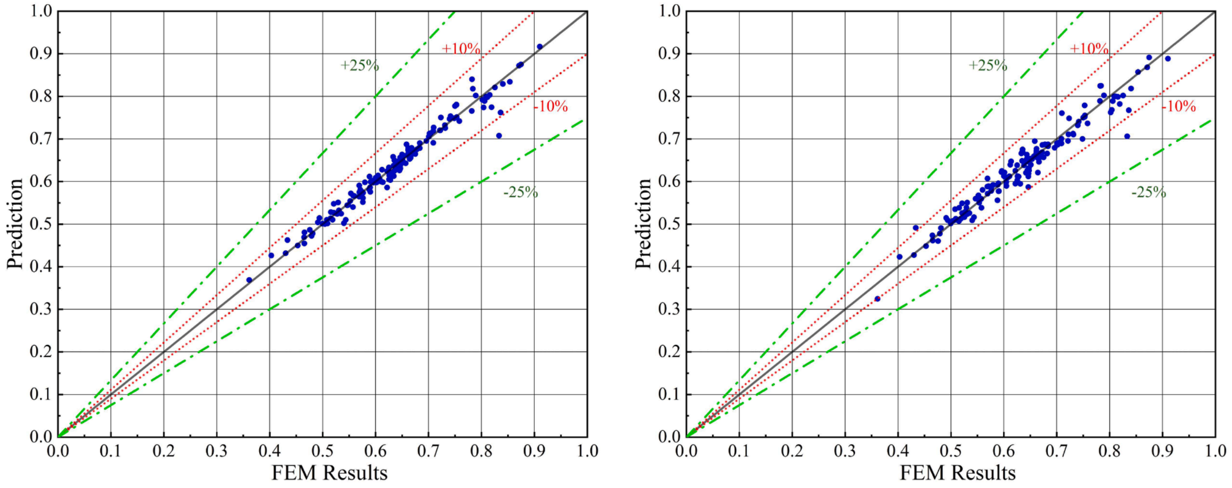

(e) Type II Model: GPR

(f) Type II Model: LSBoost

Fig. 19. Prediction accuracies of the machine learning models.

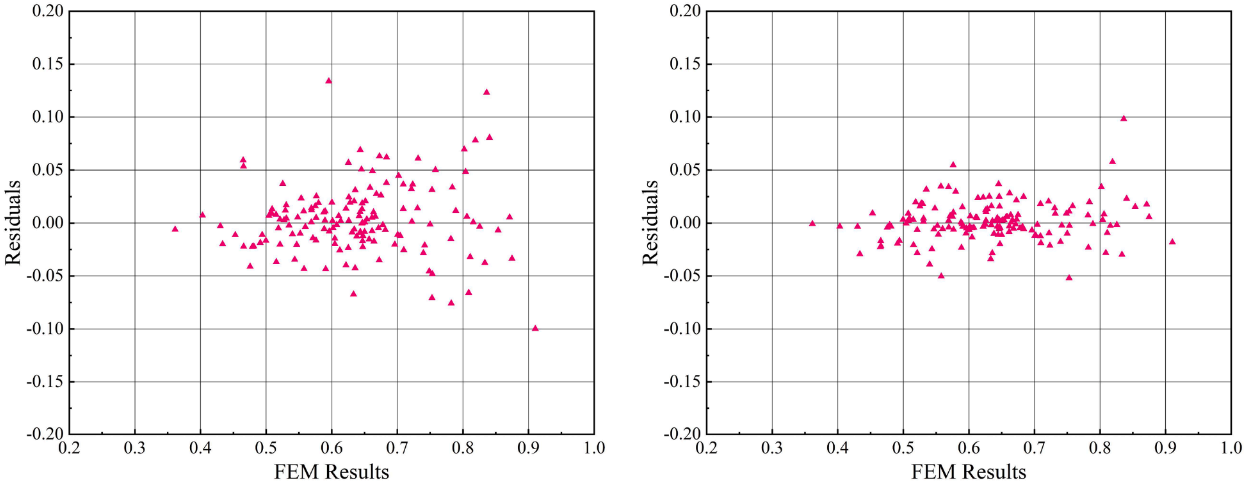

(a) Type I Model: SVM

(b) Type I Model: GPR

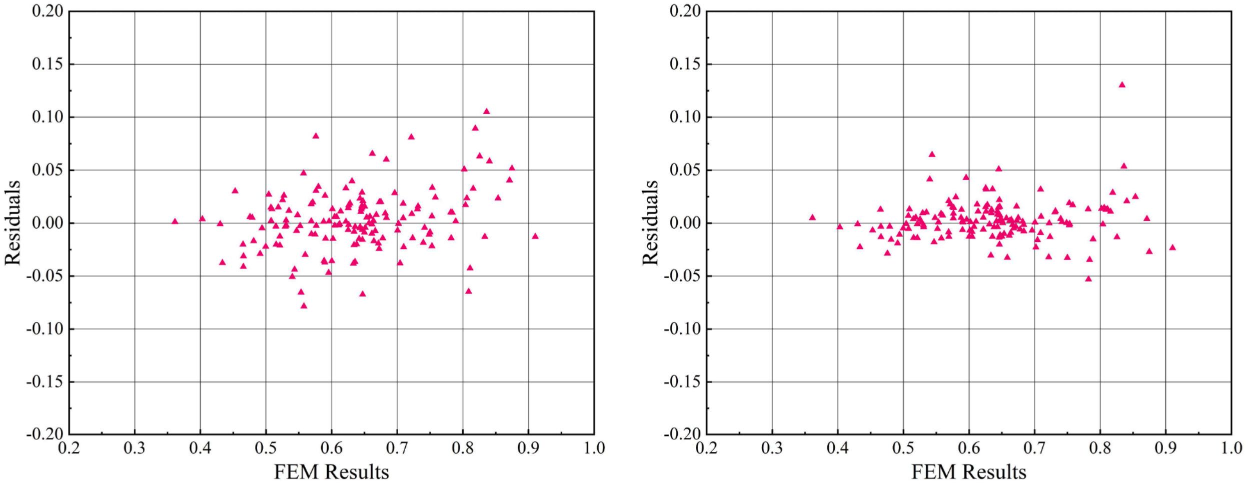

(c) Type I Model: LSBoost

(d) Type II Model: SVM

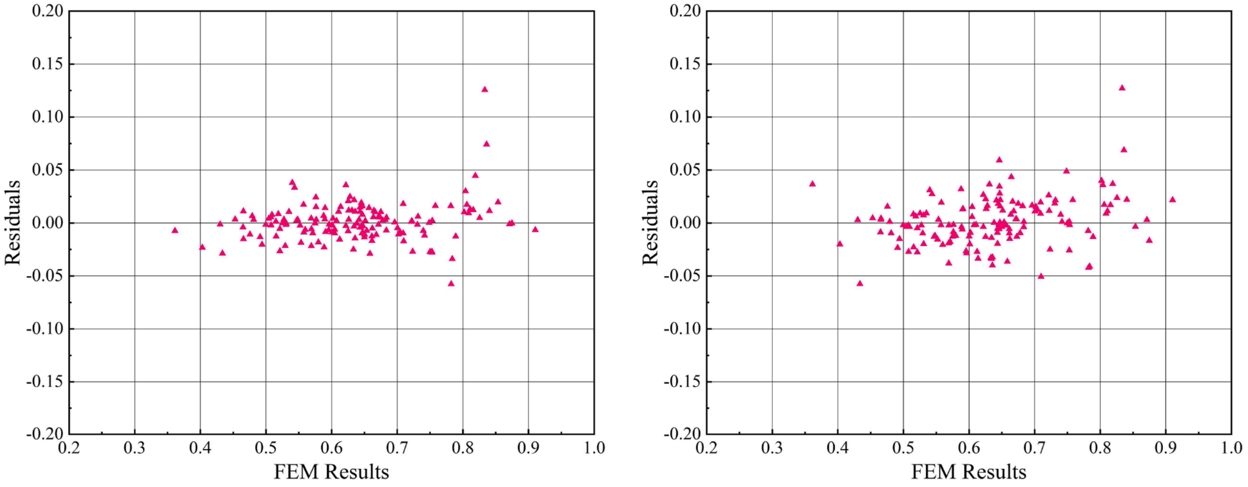

(e) Type II Model: GPR

(f) Type II Model: LSBoost

Fig. 20. Prediction residuals of the machine learning models.

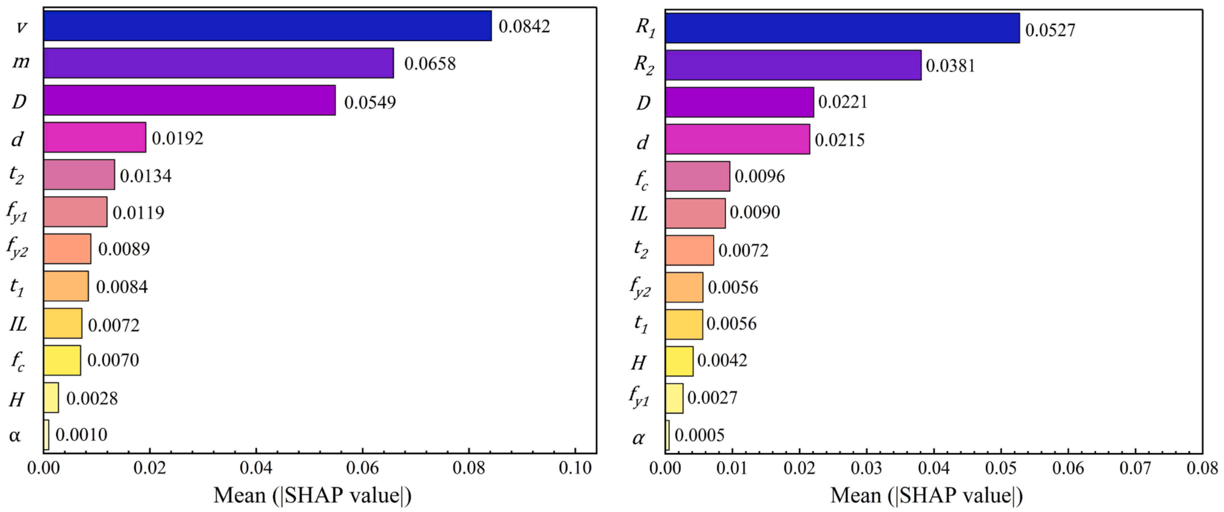

(a) Type I Model: GPR

(b) Type II Model: GPR

Fig. 21. Feature importance of GPR-based machine learning models.

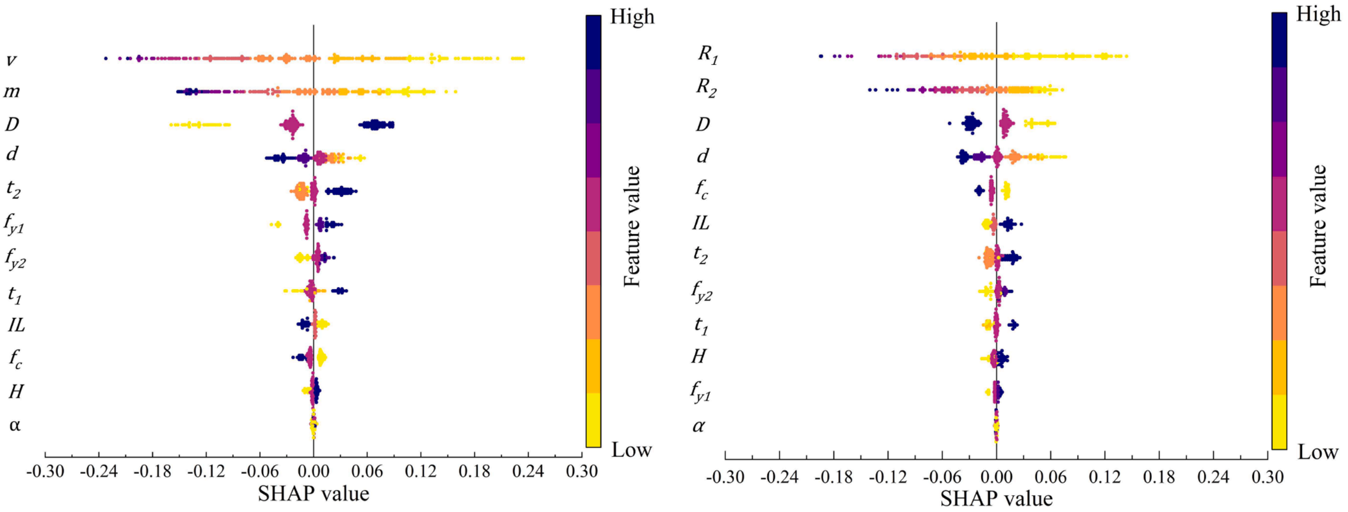

(a) Type I Model: GPR

(b) Type II Model: GPR

Fig. 22. SHAP summary plot of GPR-based machine learning models.

6. Conclusions

The residual behaviour and damage assessment of UHPC-filled DST columns after lateral impact were extensively investigated using the experiment, numerical simulation, and machine learning techniques. Drawing from these findings, the following conclusions can be given:

(1) The axial stiffness and axial load capacity are significantly decreased owing to the lateral impact for the UHPC-filled DST columns. Increasing the outer and inner steel tubes' thicknesses can increase the columns' residual axial load capacities, and the presence of axial force can also moderately increase the residual axial load capacity.

(2) The impact resistance mechanism of UHPC-filled DST columns exhibits notable variations depending on the impact location. Generally, when the impact occurs closer to the column's bottom, it results in higher peak and plateau impact forces, a shorter plateau stage, smaller global deflection, and more pronounced localized deflection.

(3) With a lower impact height, the lateral deflection difference of impacted section is significant, while the lateral deflection difference is insignificant in other regions. For the hollow concrete column, mere consideration of global deflection is unable to accurately predict the damage of impacted columns. To accurately evaluate the impact damage of hollow concrete columns, two damage indexes, one considers the global residual deflection effect (R_1), and the other considers the local residual deflection effect (R_2), should be combinedly used.

(4) Two types of machine learning-based models are developed to predict the impact damage of UHPC-filled DST columns, using GPR, SVM and LSBoost methods. Compared to SVM and LSBoost, GPR can provide the best prediction accuracies. Moreover, the SHAP method indicates that the impact mass and impact velocity are the most important input parameters for the Type I model,

while the two damage indexes R_1 and R_2 are the most important input parameters for the Type II model.

CRediT authorship contribution statement

Weiqiang Wang: Writing – review & editing, Investigation, Funding acquisition, Formal analysis, Conceptualization. **Zhilong Xiong:** Writing – original draft, Methodology, Investigation. **Yang Yu:** Writing – review & editing, Validation, Formal analysis, Conceptualization. **Da Chen:** Writing – review & editing. **Chengqing Wu:** Validation, Supervision, Project administration.

Declaration of competing interest

The authors declare that they have no known competing financial interests or personal relationships that could have appeared to influence the work reported in this paper.

Acknowledgments

The authors would like to acknowledge the financial support from the Natural Science Foundation of Jiangsu Province (No. BK20220986) and the Fundamental Research Funds for the Central Universities (No. B220201029).

Data availability

Data will be made available on request.

References

[1] L.H. Han, W. Li, R. Bjorhovde, Developments and advanced applications of concrete-filled steel tubular (CFST) structures: members, J. Constr. Steel. Res. 100 (2014) 211–228.
[2] F. Cheng, L.H. Han, W. Li, Analytical behaviour of CFDST stub columns with external stainless steel tubes under axial compression, Thin Walled Struct. 127 (2018) 756–768.
[3] W. Liang, J.F. Dong, QY. Wang, Mechanical behaviour of concrete-filled double-skin steel tube (CFDST) with stiffeners under axial and eccentric loading, Thin Walled Struct. 138 (2019) 215–230.
[4] K.Y. Jin, X.H. Zhou, W.D. Ji, R. Deng, Y.H. Wang, W. Ren, Experimental study of large-scale stiffened thin-walled CFDST columns under axial compression, Eng. Struct. 291 (2023) 116418.
[5] F. Wang, B. Young, L. Gardner, CFDST sections with square stainless steel outer tubes under axial compression: experimental investigation, numerical modelling and design, Eng. Struct. 207 (2020) 110189.
[6] X.F. Yan, Y.G. Zhao, S. Lin, Compressive behaviour of circular CFDST short columns with high-and ultrahigh-strength concrete, Thin Walled Struct. 164 (2021) 107898.
[7] X. Liu, H. Xu, X. Wang, B. Wang, L. Ma, Flexural behaviour of concrete-filled double-skin steel tubular beams after subject to high temperature, J. Constr. Steel. Res. 175 (2020) 106324.
[8] R. Deng, X.H. Zhou, W.D. Ji, R.F. Li, S.Q. Zheng, YH. Wang, Coupled behaviour and strength prediction of tapered CFDST columns with large hollow ratios for wind turbine towers, Eng. Struct. 289 (2023) 116287.
[9] M. Li, L. Wang, Y. Lin, Z. Zong, X. Zhang, Experimental study on the residual seismic performance of CFDST columns after contact explosion, Thin Walled Struct. 190 (2023) 110973.
[10] L.H. Han, D. Lam, D. Nethercot, Design Guide for Concrete-Filled Double Skin Steel Tubular Structures, CRC Press, 2018.
[11] D.Y. Yoo, N. Banthia, Mechanical properties of ultra-high-performance fiber-reinforced concrete: a review, Cem. Concr. Compos. 73 (2016) 267–280.
[12] D. Fan, Y. Rui, K. Liu, J. Tan, Z. Shui, C. Wu, S. Wang, Z. Guan, Z. Hu, Q. Su, Optimized design of steel fibres reinforced ultra-high performance concrete (UHPC) composites: Towards to dense structure and efficient fibre application, Constr. Build. Mater. 273 (2021) 121698.
[13] B. Yang, L. Shen, K. Chen, C. Feng, X. Lin, M. Elchalakani, S. Xu, Mechanical performance of circular ultrahigh-performance concrete–filled double skin high-strength steel tubular stub columns under axial compression, J. Struct. Eng. 148 (3) (2022):04021298.
[14] L. Shen, B. Yang, M. Ding, C. Feng, D. Wang, M. Liu, M. Elchalakan, Experimental and numerical studies on the axial compression performance of hexagonal stiffened CFDST stub columns, Compos. Struct. 311 (2023) 116801.
[15] H. Zhao, R. Wang, C.C. Hou, D. Lam, Performance of circular CFDST members with external stainless steel tube under transverse impact loading, Thin Walled Struct. 145 (2019) 106380.
[16] S. Pan, J. Guo, Numerical study on dynamic responses and residual axial bearing capacity of square CFDST columns under lateral impact, J. Constr. Steel Res. 213 (2024) 108427.
[17] Q. Yan, J. Zhang, Z. Ma, F. Liu, H. Song, G. Zhao, C. Gu, Experimental and theoretical investigation on residual bearing capacity of CFDST-T joints after lateral impact, J. Build. Eng. 84 (2024) 108462.
[18] Z. Zhang, W. Chen, K. Wang, X. Guo, Concrete-filled double steel tubular beams under lateral impact, Case Stud. Constr. Mater. 17 (2022) e01252.
[19] X. Wei, W. Chen, H. Hao, W.D. Wang, R. Wang, Investigation on the lateral impact responses of circular concrete-filled double-tube (CFDT) members, Compos. Struct. 255 (2021) 112993.
[20] J. Li, W. Wang, C. Wu, Z. Liu, P. Wu, Impact response of ultra-high performance fiber-reinforced concrete filled square double-skin steel tubular columns, Steel Compos. Struct. 42 (3) (2022) 325–351.
[21] R. Wang, L.H. Han, X.L. Zhao, J.R. Rasmussen Kim, Experimental behaviour of concrete filled double steel tubular (CFDST) members under low velocity drop weight impact, Thin Walled Struct. 97 (2015) 279–295.
[22] Y.F. Yang, Z.C. Zhang, F. Fu, Experimental and numerical study on square RACFST members under lateral impact loading, J. Constr. Steel Res. 111 (2015) 43–56.
[23] W. Wang, C. Wu, J. Li, Z. Liu, Y. Lv, Behaviour of ultra-high performance fibre-reinforced concrete (UHPFRC) filled steel tubular members under lateral impact loading, Int. J. Impact Eng. 132 (2019) 103314.
[24] Y. Wang, X. Qian, J.Y. Richard Liew, M.H. Zhang, Experimental behaviour of cement filled pipe-in-pipe composite structures under transverse impact, Int. J. Impact Eng. 72 (2014) 1–16.
[25] R. Wang, L.H. Han, X.L. Zhao, J.R. Rasmussen Kim, Analytical behaviour of concrete filled double steel tubular (CFDST) members under lateral impact, Thin Walled Struct. 101 (2016) 129–140.
[26] S. Aghdamy, D.P. Thambiratnam, M. Dhanasekar, S. Saiedi, Effects of load-related parameters on the response of concrete-filled double-skin steel tube columns subjected to lateral impact, J. Constr. Steel Res. 138 (2017) 642–662.
[27] W. Wang, C. Wu, J. Li, Z. Liu, X. Zhi, Lateral impact behaviour of double-skin steel tubular (DST) members with ultra-high performance fiber-reinforced concrete (UHPFRC), Thin Walled Struct. 144 (2019) 106351.
[28] W. Fan, B. Liu, GR. Consolazio, Residual capacity of axially loaded circular RC columns after lateral low-velocity impact, J. Struct. Eng. 145 (6) (2019) 04019039.
[29] S. Gao, Y. Xu, S. Zhang, A. Derlatka, Performance of square concrete-filled steel tubular columns under repeated lateral impact, Eng. Struct. 280 (2023) 115719.
[30] R. Wang, X. Yang, H. Zhao, M. Zhai, W. Chen, L. Dennis, Damage evaluation of axial-loaded H-section steel columns during and after impact loading, J. Constr. Steel Res. 196 (2022) 107426.
[31] J. Wei, J. Li, C. Wu, An experimental and numerical study of reinforced conventional concrete and ultra-high performance concrete columns under lateral impact loads, Eng. Struct. 201 (2019) 109822.
[32] M. Almustafa, M. Nehdi, Machine learning model for predicting structural response of RC columns subjected to blast loading, Int. J. Impact Eng. 162 (2022) 104145.
[33] J. Li, Y. Pang, Q. Mu, X. Zhang, Y. Shi, H. Wang, Post-blast capacity evaluation of concrete-filled steel tubular (CFST) column based on machine learning technique, Adv. Struct. Eng. 26 (2023) 1953–1972.
[34] J. Li, Y. Pang, K. Wang, X. Zhang, N. Wang, Explainable machine-learning model for rapid damage assessment of CFST columns after close-in explosion, J. Perform. Constr. Facil. 38 (3) (2024) 04024010.
[35] Z.X. Li, X. Zhang, Y. Shi, C. Wu, J. Li, Predication of the residual axial load capacity of CFRP-strengthened RC column subjected to blast loading using artificial neural network, Eng. Struct. 242 (2021) 112519.
[36] X.Q. Zhou, B.G. Huang, X.Y. Wang, Y. Xia, Deep learning-based rapid damage assessment of RC columns under blast loading, Eng. Struct. 271 (2022) 114949.
[37] C. Zhou, Y. Xie, W. Wang, Y. Zheng, Machine learning driven post-impact damage state prediction for performance-based crashworthiness design of bridge piers, Eng. Struct. 292 (2023) 116539.
[38] G. Xu, Z. Gao, J. Wang, S. Xue, M. Tang, A novel machine learning-based framework for predicting impact force in ship-bridge pier collisions, Ocean Eng. 285 (2023) 115347.
[39] AS (Australian Standard), Methods of testing concrete—method 9: determination of the compressive strength of concrete specimens[J], 2014.
[40] British Standards Institution. Method for Tensile Testing of Metals (including Aerospace Materials)[M], British Standards Institution, 1987.
[41] Manual L S D K U. Livermore Software Technology Corporation: Livermore[J], CA, USA, 1998.
[42] X. Yin, Q. Li, X. Xu, B. Chen, K. Guo, S. Xu, Investigation of continuous surface cap model (CSCM) for numerical simulation of strain-hardening fibre-reinforced cementitious composites against low-velocity impacts, Compos. Struct. 304 (2023) 116424.
[43] K. Liu, C. Wu, X. Li, Q. Li, J. Fang, J. Liu, A modified HJC model for improved dynamic response of brittle materials under blasting loads, Comput. Geotech. 123 (2020) 103584.
[44] Q. Su, H. Wu, Q. Fang, Calibration of KCC model for UHPC under impact and blast loadings, Cem. Concr. Compos. 127 (2022) 104401.
[45] S. Xu, P. Wu, Z. Liu, C. Wu, Calibration of CSCM model for numerical modeling of UHPCFTWST columns against monotonic lateral loading, Eng. Struct. 240 (2021) 112396.
[46] Y. Wei, YF. Wu, Experimental study of concrete columns with localized failure, J. Compos. Constr. 20 (5) (2016) 04016032.
[47] Technical Standard for Concrete-filled Steel Tubular (CFST) Hybrid Structure. Ministry of Housing and Urban-Rural Development of the People's Republic of China, Beijing, China, 2021.

[48] X. Bao, B. Li, Residual strength of blast damaged reinforced concrete columns, Int. J. Impact Eng. 37 (3) (2010) 295–308.

[49] J. Cui, Y. Shi, Z.X. Li, L. Chen, Failure analysis and damage assessment of RC columns under close-in explosions, J. Perform. Constr. Facil. 29 (5) (2015) B4015003.

[50] W. Wang, C. Wu, Y. Yu, J.J. Zeng, Dynamic responses of hybrid FRP-concrete-steel double-skin tubular column (DSTC) under lateral impact, Structures 32 (2021) 1115–1144.

[51] Lundberg S. A unified approach to interpreting model predictions[J]. arXiv preprint arXiv:1705.07874, 2017.